Model of Gamma Frequency Burst Discharge Generated by Conditional Backpropagation

BRENT DOIRON,[1] ANDRÉ LONGTIN,[1] RAY W. TURNER,[2] AND LEONARD MALER[3]

[1]*Physics Department, University of Ottawa, Ottawa, Ontario K1N 6N5;* [2]*Department of Cell Biology and Anatomy, Neuroscience Research Group, University of Calgary, Calgary, Alberta T2N 4N1; and* [3]*Department of Cellular and Molecular Medicine, University of Ottawa, Ottawa, Ontario K1H 8M5, Canada*

Doiron, Brent, André Longtin, Ray W. Turner, and Leonard Maler. Model of gamma frequency burst discharge generated by conditional backpropagation. *J Neurophysiol* 86: 1523–1545, 2001. Pyramidal cells of the electrosensory lateral line lobe (ELL) of the weakly electric fish *Apteronotus leptorhynchus* have been shown to produce oscillatory burst discharge in the γ-frequency range (20–80 Hz) in response to constant depolarizing stimuli. Previous in vitro studies have shown that these bursts arise through a recurring spike backpropagation from soma to apical dendrites that is conditional on the frequency of action potential discharge ("conditional backpropagation"). Spike bursts are characterized by a progressive decrease in inter-spike intervals (ISIs), and an increase of dendritic spike duration and the amplitude of a somatic depolarizing afterpotential (DAP). The bursts are terminated when a high-frequency somatic spike doublet exceeds the dendritic spike refractory period, preventing spike backpropagation. We present a detailed multi-compartmental model of an ELL basilar pyramidal cell to simulate somatic and dendritic spike discharge and test the conditions necessary to produce a burst output. The model ionic channels are described by modified Hodgkin-Huxley equations and distributed over both soma and dendrites under the constraint of available immunocytochemical and electrophysiological data. The currents modeled are somatic and dendritic sodium and potassium involved in action potential generation, somatic and proximal apical dendritic persistent sodium, and $K_V 3.3$ and fast transient A-like potassium channels distributed over the entire model cell. The core model produces realistic somatic and dendritic spikes, differential spike refractory periods, and a somatic DAP. However, the core model does not produce oscillatory spike bursts with constant depolarizing stimuli. We find that a cumulative inactivation of potassium channels underlying dendritic spike repolarization is a necessary condition for the model to produce a sustained γ-frequency burst pattern matching experimental results. This cumulative inactivation accounts for a frequency-dependent broadening of dendritic spikes and results in a conditional failure of backpropagation when the intraburst ISI exceeds dendritic spike refractory period, terminating the burst. These findings implicate ion channels involved in repolarizing dendritic spikes as being central to the process of conditional backpropagation and oscillatory burst discharge in this principal sensory output neuron of the ELL.

INTRODUCTION

The temporal discharge pattern of central neurons is an important element of signal processing and information transfer. Cortical neurons have traditionally been grouped into three broad classes according to their discharge patterns in response to depolarizing current injection: regular spiking, fast spiking, and intrinsic bursting (Connors and Gutnick 1990; Connors et al. 1982; McCormick et al. 1985). Both regular and fast spiking cells respond to depolarizing current with a repetitive discharge of action potentials but differ in that regular spiking neurons show significant frequency adaptation in their firing pattern compared with the consistent discharge frequency of fast spiking cells. However, the discharge pattern of intrinsic bursting neurons is quite distinct in generating a phasic burst followed by a tonic discharge of action potentials. Several studies have focused on distinguishing morphological and electrophysiological characteristics of neurons exhibiting these three patterns of spike output (Franceschetti et al. 1995; Jensen et al. 1994; Mason and Larkman 1990; Nuñez et al. 1993; Schwindt et al. 1997; Williams and Stuart 1999). A fourth discharge pattern consisting of rhythmic spike bursts in the γ-frequency range (20–80 Hz) has now been identified in cortical as well as sub-cortical and medullary neurons (Brumburg et al. 2000; Gray and McCormick 1996; Lemon and Turner 2000; Lo et al. 1998; Paré et al. 1995; Steriade et al. 1998; Turner et al. 1994). This pattern differs from intrinsic bursting cells by exhibiting a continuous and nonadapting series of spike bursts during current injection (Gray and McCormick 1996; Steriade et al. 1998; Turner et al. 1994).

Gamma frequency discharge is thought to be important to several aspects of signal processing and neuronal synchronization (Gray and McCormick 1996; Gray and Singer 1989; Lisman 1997; Ribary et al. 1991), yet comparatively few studies have examined the mechanisms underlying burst output at such a high-frequency. Gamma frequency bursting in hippocampus is known to involve extensive interneuronal synaptic circuitry (Buzsáki and Chrobak 1995; Stanford et al. 1998; Traub et al. 1998). Other studies have revealed that backpropagating dendritic spikes contribute to burst discharge by generating a depolarizing afterpotential (DAP) at the soma (Mainen and Sejnowski 1996; Turner et al. 1994; Wang 1999; Williams and Stuart 1999). The amplitude of the DAP can be augmented by a persistent sodium current (I_{NaP}) (Brumburg et al. 2000; Franceschetti et al. 1995; Wang 1999) or dendritic Ca^{2+} cur-

---

rent (Magee and Carruth 1999; Williams and Stuart 1999). Alternatively, the amplitude of the DAP can be influenced by dendritic morphology because the dendrite-to-soma current flow increases with the relative dendritic to somatic surface area and decreases with axial resistance (Mainen and Sejnowski 1996; Quadroni and Knofnel 1994). Lemon and Turner (2000) recently described a novel mechanism of "conditional spike backpropagation" that modulates DAP amplitude and produces a γ-frequency oscillatory burst discharge in pyramidal neurons of the electrosensory system.

Electrosensory lateral line lobe (ELL) pyramidal cells are principal output cells in the medulla that respond to AM of electric fields detected by peripheral electroreceptors (Bastian 1981; Shumway 1989). Several studies have described the properties of burst discharge in ELL pyramidal cells (Bastian and Nguyenkim 2001; Gabbiani and Metzner 1999; Gabbiani et al. 1996; Lemon and Turner 2000; Metzner et al. 1998; Rashid et al. 2001; Turner and Maler 1999; Turner et al. 1994, 1996). Signal detection analysis has shown that ELL pyramidal cells generate burst discharge in relation to specific signal features, such as up or down strokes in the external electric field (Gabbiani and Metzner 1999; Gabbiani et al. 1996; Metzner et al. 1998). Further, significant progress has been made in identifying how conditional backpropagation generates an oscillatory pattern of spike bursts in ELL pyramidal cells in vitro. Pyramidal cell spike bursts are initiated when a Na^+ spike backpropagating over the initial 200 μm of apical dendrites generates a somatic DAP (Turner et al. 1994). A frequency-dependent broadening of dendritic spikes potentiates the DAP until a high-frequency spike doublet is triggered at the soma (Lemon and Turner 2000). The short inter-spike interval (ISI) of the doublet falls within the dendritic refractory period and blocks spike backpropagation, removing the dendritic depolarization that drives the burst. Repetition of this conditional process of backpropagation groups repetitive spike discharges into bursts in the γ-frequency range. A key issue that remains in understanding the mechanism of ELL burst discharge is the identity of factor(s) underlying the frequency-dependent broadening of dendritic spikes that drives burst discharge.

Our present knowledge of spike discharge in ELL pyramidal cells and the simple mechanism underlying conditional backpropagation provides an excellent opportunity to model a form of γ-frequency burst discharge and test hypotheses about burst generation. This study presents a detailed compartmental model of an ELL pyramidal cell that is based on extensive electrophysiological and morphological data. We establish the distribution and complement of ion channels that are necessary to fit various aspects of Na^+ spike discharge and spike backpropagation to physiological data. However, the resulting model neuron fails to reproduce the change in dendritic spike repolarization and somatic afterpotentials required to induce γ-frequency bursting. Hence we test potential ionic mechanisms that could underlie burst discharge. Our results show that cumulative inactivation of a dendritic K^+ current is necessary and sufficient to generate a burst discharge that is remarkably similar to that found in ELL pyramidal cells in vitro. Some of this work has been previously reported in abstract form (Doiron et al. 2000).

METHODS

The compartmental model we use in this investigation builds on the earlier one introduced in Doiron et al. (2001). Simulations are performed with the software package NEURON (Hines and Carnevale 1997), which uses a central difference algorithm (Crank-Nicholson) to integrate forward in time. The time step for all simulations is 0.025 ms, well below the time scale of the synaptic and ionic responses present in the ELL (Berman and Maler 1999; Berman et al. 1997).

Cell morphology and discretization

Pyramidal cell somata are located within a pyramidal cell body layer, a distinct lamina in the ELL. Basal and apical dendrites emanate from the ventral and dorsal aspects of the cell soma, respectively; the basal dendrites receive electrosensory afferent input while the apical dendrites receive feedback input (Berman and Maler 1999). There are two classes of pyramidal cells, basilar and nonbasilar (lacking a basal dendrite), both of which generate γ-frequency oscillatory spike bursts that depend on conditional backpropagation into the apical dendrites (Lemon and Turner 2000; Turner et al. 1994). The present model is focused on the activity associated with basilar pyramidal cells to allow future analysis of the effect of electrosensory afferent input on burst discharge.

Figure 1 shows our two-dimensional spatial compartmentalization of a basilar pyramidal neuron based on detailed spatial measurements of confocal images of a Lucifer yellow-filled neuron (Berman et al. 1997). The model contains 153 compartments with lengths ranging from 0.8 to 669.2 μm and diameters spanning from 0.5 to 11.6 μm.
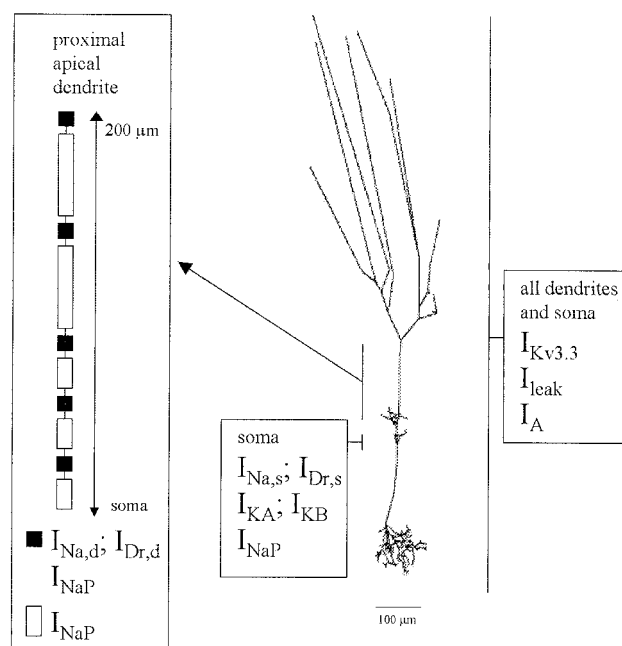

FIG. 1. Basilar pyramidal cell morphology and ionic channel distribution incorporated into the compartmental model. Typical basilar pyramidal cells have somata of 10–25 μm in diameter; a basilar dendritic trunk of 5–12 μm in diameter extending 200–400 μm distance before branching to form a distal basilar bush (Maler 1979). A thick proximal apical dendritic shaft of ~10 μm in diameter extends dorsally ~200 μm prior to branching in a molecular layer; the apical dendrites continue to branch over a distance of ≤800 μm. The particular pyramidal cell used for the model was reconstructed from a Lucifer-yellow filled cell (Berman et al. 1997). The distribution of ionic channels in the core model is indicated in 3 boxes according to their location on the soma, proximal apical dendrite, or all dendrites, respectively. An enlargement of the proximal apical dendrite is shown on the *left* to detail the placement of Na^+ and K^+ channels in separate proximal dendritic compartments over the region for backpropagation of dendritic Na^+ spikes.

The total model cell surface area is 65,706 μm^2, comparable to other pyramidal cell models (Koch et al. 1995). Longer compartments are further subdivided to guarantee that no isopotential segment is of length >25 μm, ensuring sufficient computational precision. This results in a total spatial discretization of the full model cell into 312 isopotential regions. For simplicity, the initial segment and soma are represented as a single compartment.

The proximal apical dendrite is modeled by ten connected compartments (total length, 200 μm) whose diameter decreases with distance from the somatic compartment (initial diameter of 11.6 mm, final diameter of 6 μm; see Fig. 1, *inset*). The dendrite then bifurcates to give rise to daughter branches of 6 μm diameter, which further bifurcate with an associated step decrease in diameter, extending a total distance of ~800 μm in an overlying molecular layer. The proximal basilar dendrite is modeled as a single compartment of 7.4 μm diameter and 194 μm in length. The distal extent of the dendrite separates into many compartments that form a bush-like pattern (see Fig. 1). The lengths of dendrites within the basilar bush range from 3 to 56 μm with diameters as thick as 4 μm to as thin as 0.5 μm. As the axial resistivity (R_a) and membrane capacitance per unit area (C_m) are not precisely known for ELL pyramidal cells, R_a is set to 250 Ωcm and C_m to 0.75 $\mu F/cm^2$, both realistic values for vertebrate neurons (Mainen and Sejnowski 1998). The model cell temperature is set to 28°C, similar to the natural habitat of the fish.

Model equations

Each ionic current, I_x, is modeled as a modified Hodgkin/Huxley channel (Hodgkin and Huxley 1952) governed by

$$I_x = g_{max,x} \cdot m_x^i h_x^j \cdot (V_m - E_{rev,x}) \qquad (1.1)$$

$$\frac{dm_x}{dt} = \frac{m_{\infty,x}(V_m) - m_x}{\tau_{m,x}} \qquad (1.2)$$

$$m_{\infty,x}(V_m) = (1 + e^{-(V_m - V_{1/2,m,x})/k_{m,x}})^{-1} \qquad (1.3)$$

h_x is given by a similar description (equations omitted). Here $g_{max,x}$ is the maximal channel conductance of a generic channel x, while m_x and h_x are the activation and inactivation state variables, raised to powers i and j, respectively. $m_{\infty,x}$ is the steady state activation curve, and $\tau_{m,x}$ the activation time constant, both governing the evolution of the variable m_x. The voltage dependence of $m_{\infty,x}$ is given by a sigmoid relationship (*Eq. 1.3*) determined by the half voltage $V_{1/2,m,x}$ and slope parameter $k_{m,x}$. The channel reversal potential is $E_{rev,x}$. To facilitate parameter fitting, our model follows Koch et al. (1995) in assuming $\tau_{m,x}$ is voltage independent.

Figure 1 introduces the specific ionic currents and indicates their distribution over the cell. Table 1 gives the parameters stated in *Eq. 1.1–1.3* for each current. In this study, "proximal dendrite" refers to the initial 200 μm of the apical dendrite, which is in most pyramidal cells a single nonbranching shaft over this distance. A detailed analysis of basilar dendritic electrophysiology is not available, hence few ionic channels are localized to the basilar dendritic region. The ionic channels (I_x) influence the potential of each compartment according to

$$C_m \frac{dV_m}{dt} = \sum_x I_x + I_{app} \qquad (2)$$

where the sum is over all the ionic currents I_x present in a given compartment as indicated in the distribution of Fig. 1. I_{app} represents an externally applied current that is always constant in time and injected into the somatic compartment for this study.

RESULTS

For each ionic channel incorporated into the model, we first justify the chosen distribution over the cell (Fig. 1) and identify the influence of each conductance on cell membrane potential. Finally, the parameters are fit so that model performance matches known experimental recordings. In the case of insufficient experimental evidence from pyramidal cells, values were taken from experimental or computational results reported for other cells.

Channel distribution and kinetics

PASSIVE CURRENT I_{LEAK}. I_{leak} represents the classic leak channel with voltage-independent conductance and is present in all compartments. The channel density, $g_{max,leak}$ is chosen to establish the model input resistance as 76.1 $M\Omega$ and the passive membrane time constant as 26.8 ms, similar to values measured in intracellular recordings of pyramidal cells in vitro (Lemon and Turner 2000). The leak reversal potential, $E_{rev,leak}$, is set to −70 mV (Koch et al. 1995; Mainen et al. 1995; Rapp et al. 1996). Due to the high-density of K$^+$ currents (see following text) the final resting membrane potential (RMP) of the core model is −73.3 mV, a value within the range recorded in pyramidal cells in vitro (Berman and Maler 1998a; Turner et al. 1994).

TABLE 1. *Model parameters*

Channel	g_{max}, S/cm^2	i/j	E_{rev}, mV	τ, ms	$V_{1/2}$, mV	k, mV
$I_{Na,s}$	1.8	2/1	40	0.2/0.6 5	−40/−45	3/−3
I_{Dr}	0.7	2/0	−88.5	0.39	−40	3
I_{KA}	0.27	1/0	−88.5	1	−30	4
I_{KB}	0.015	1/0	−88.5	2000	−30	1
$I_{KV3.3}$	6.5: soma. 1: proximal apical dendrite. 0.5: basal and distal apical dendrite.	3/1	−88.5	0.8/1.5	0/−3	19/−40
I_{NaP}	0.0035: soma. 0.001: proximal apical dendrite.	3 3	40 40	0.3 0.3	−58.5 −58.5	6 6
$I_{Na,d}$	0.6	2/1	40	0.5/1	−40/−52	5/−5
I_A	0.0012	1/1	−88.5	10/100	−75/−85	4/−2
$I_{Dr,d}$	0.2	2/0	−88.5	0.9	−40	5
I_{Leak}	2 10^{-5}	N/A	−70	N/A	N/A	N/A

Ionic channel parameters. All parameters correspond to the notation given in *Eqs. 1.1–1.3*. If the channel is present, and of varying density, in multiple compartments (see Fig. 1), the density for the specific compartments is indicated in column 2. If the channel is modeled with both activation and inactivation associated entries will be double; the left is associated with activation parameters and the left with inactivation parameters.

Na$^+$ AND K$^+$ CURRENTS. Previous work has established the distribution pattern of immunolabel for both Na$^+$ channels and an apteronotid homologue of the Kv3.3 K$^+$ channel, *Apt*Kv3.3, over the dendritic-somatic axis of pyramidal cells (Rashid et al. 2001; Turner et al. 1994). Electrophysiological studies have further mapped the site for Na$^+$ spike initiation and conduction over the soma-dendritic axis (Lemon and Turner 2000; Turner et al. 1994) and identified the kinetic properties of *Apt*Kv3.3 K$^+$ channels in both native pyramidal cells and when expressed in a heterologous expression system (Rashid et al. 2001). Although other K$^+$ channels are incorporated into the model, our existing knowledge of the distribution and properties of Na$^+$ and *Apt*Kv3.3 K$^+$ channels are used when possible to constrain our parameters and improve the representation of action potential waveforms. We begin by matching the distribution and kinetic properties of *Apt*Kv3.3 channels to experimental data.

$I_{AptKv3.3}$: high-voltage-activated K$^+$ channel

*Apt*Kv3.3 K$^+$ channels are distributed over ELL pyramidal cell somata as well as apical and basal dendrites (Rashid et al. 2001). A dendritic distribution of *Apt*Kv3.3 channels is unique in that all previous studies on Kv3 channels have shown a distribution that is restricted to the soma, axon, and presynaptic terminals (Perney and Kaczmarek 1997; Sekirnjak et al. 1997; Weiser et al. 1995). Rashid et al. (2001) also showed that *Apt*Kv3.3 K$^+$ channels contribute to spike repolarization in both somatic and apical dendritic membranes. This role is particularly relevant in dendritic regions where a reduction in *Apt*Kv3.3 current enhances the somatic DAP and lowers burst threshold.

Figure 2 shows the fit of *Apt*Kv3.3 current in the model to whole cell recordings of *Apt*Kv3.3 K$^+$ current when expressed in human embryonic kidney (HEK) cells. *Apt*Kv3.3 channels produce an outwardly rectifying current that exhibits a high-threshold voltage for initial activation (more than -20 mV; Fig. 2, *A* and *B*). Over a 100-ms time frame, step commands produce little inactivation of *Apt*Kv3.3 current in the whole cell recording configuration (Fig. 2*A*), although inactivation can be recorded over longer time frames (Rashid et al. 2001). As indicated in Table 1, both activation ($m_{AptKv3.3}$) and inactivation ($h_{AptKv3.3}$) curves are used to describe $I_{AptKv3.3}$. The $V_{1/2}$ for $m_{AptKv3.3}$ is set to 0 mV so as to produce the high-threshold voltage necessary for activation as shown in Fig. 2*B*. A shallow slope of activation, $k_{m,AptKv3.3}$, is required to produce a gradual rise of $I_{AptKv3.3}$ with voltage.

As reported for Kv3 channels in some expression systems, *Apt*Kv3.3 current exhibits an early peak on initial activation followed by a relaxation to a lower amplitude current for the duration of a 100-ms step command (Fig. 2*A*). The origin of this early peak and relaxation is currently unknown, but it has been proposed to reflect a transient accumulation of extracellular K$^+$ when Kv3 channels are expressed at high-density in expression systems (Rudy et al. 1999). Since this has not been firmly established, we incorporate inactivation kinetics ($V_{1/2,h,AptKv3.3}$, $k_{h,AptKv3.3}$, $\tau_{h,AptKv3.3}$) that allow the model to reproduce the early transient peak of current (Fig. 2*A*). An additional characteristic of Kv3 channels is a fast rate of both activation and deactivation (Fig. 2*C*). The activation time constant, $\tau_{m,Kv3.3}$, is chosen to produce rates of activation and deactivation that most closely match the experimental data
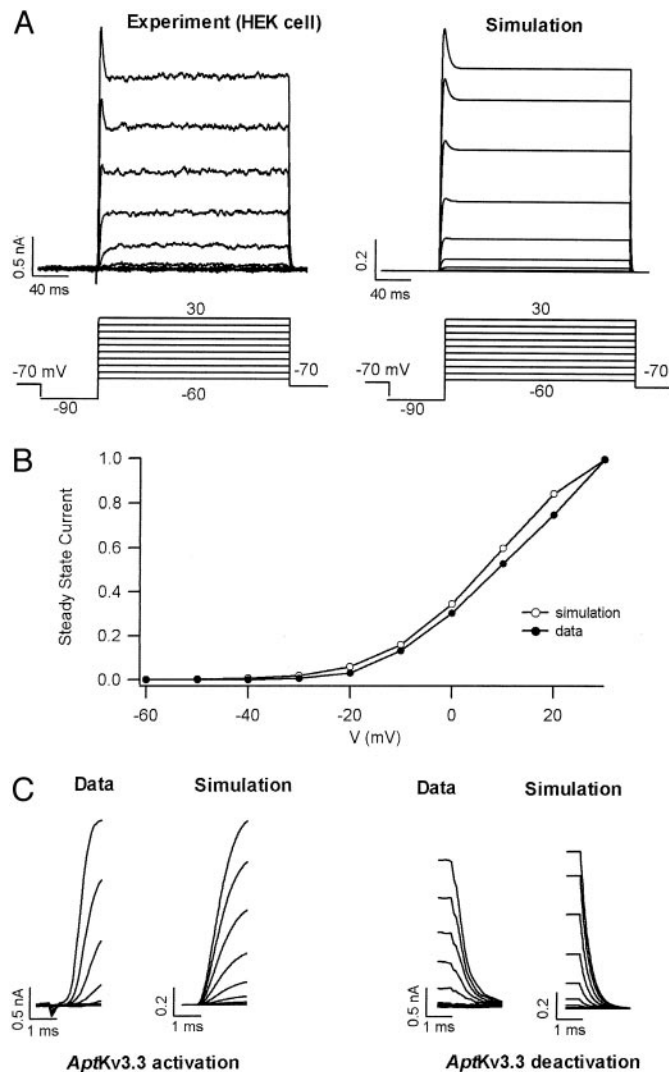

FIG. 2. *Apt*Kv3.3 K$^+$ channel kinetics. *A*: whole cell K$^+$ currents recorded in tsA 201 HEK cells transiently transfected with *Apt*Kv3.3 K$^+$ channels (*left*). Shown are currents activated by step commands in 10-mV increments from an initial prepotential of -90 mV. Model *Apt*Kv3.3 currents (*right*) in response to an equivalent voltage-clamp protocol as the experimental recordings in *A*, restricted to the somatic compartment for space-clamp considerations. Simulated *Apt*Kv3.3 whole cell currents shown here and in *C* have calibration bars normalized to the current evoked at 30 mV. We normalize the simulation results because we do not wish to quantitatively compare the simulation to the HEK cell experiments. *B*: normalized current-voltage plots for both experimental and model *Apt*Kv3.3 currents in response to the voltage-clamp protocol shown in *A*. A high initial voltage for activation of *Apt*Kv3.3 current is evident in that whole cell current becomes significant only for voltage steps above -20 mV. *C*: time expanded plots of the beginning and end of *Apt*Kv3.3 whole cell currents in response to the voltage steps shown in *A*. This shows both the fast activation and deactivation of *Apt*Kv3.3 current. See Rashid et al. (2001) for a description of experimental methods.

(Fig. 2*C*). Because *Apt*Kv3.3 channels are found with high prevalence in the soma and dendrites, they are incorporated with the above kinetics over the entire axis of the model cell (Fig. 1). The conductance level is adjusted accordingly to the fit to experimental data (see following text).

Action potential discharge in ELL pyramidal cells

We first treat somatic and dendritic spike discharge separately to determine the necessary descriptions of the model
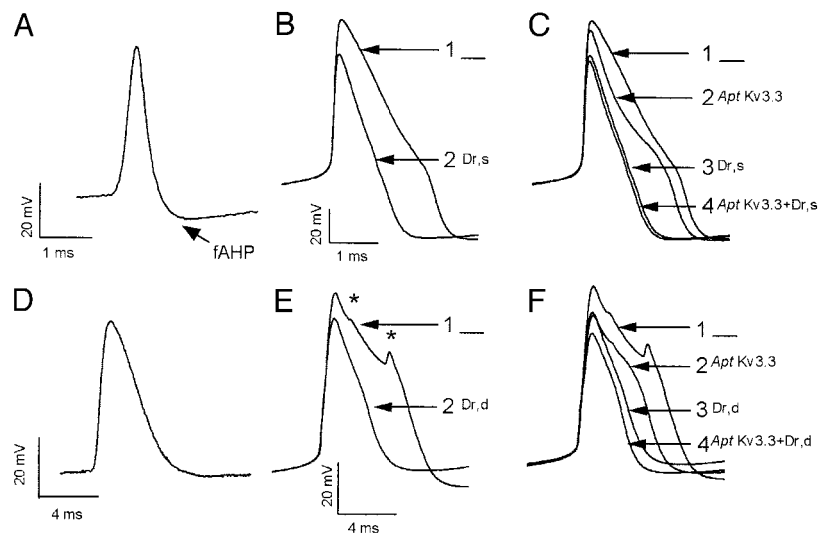
FIG. 3. Fit of somatic and dendritic spikes to experimental data. *A*: in vitro recording of an electrosensory lateral line lobe (ELL) pyramidal cell somatic action potential under conditions of complete block of all spike backpropagation by dendritic TTX application (Lemon and Turner 2000). This serves to selectively remove the depolarizing afterpotential (DAP) from the somatic recording, unmasking a large fast afterhyperpolarization (fAHP). *B* and *C*: superimposed simulations comparing the effects of various combinations of K^+ currents on the rate of somatic spike repolarization. All simulations have KA and KB channels present at the soma and Na,d channels have been removed to block backpropagation. All action potentials are produced via a square wave step depolarization for I_{app} at the soma (amplitude of 0.3 nA, 0.5 ms in duration). *B*: insertion of $I_{Dr,s}$ at the soma results in a substantial increase in the rate of spike repolarization with an associated decrease in spike height (trace 1 vs. trace 2). *C*: a series of superimposed simulations to illustrate the effects of combining $I_{Dr,s}$ and $I_{AptKv3.3}$ on spike repolarization. The results show that $I_{AptKv3.3}$ alone affects primarily the initial falling phase of the spike but only a fraction of the total repolarization (trace 1 vs. 2). The best fit is obtained by combining $I_{Dr,s}$ and $I_{AptKv3.3}$ (trace 4). Trace 3 indicates that subsequent removal of $I_{AptKv3.3}$ at the soma has a moderate effect on spike repolarization but little effect on spike amplitude. *D*: in vitro recording of an ELL pyramidal cell dendritic spike ($\sim$150 μm). Note the slower rate of rise, lower amplitude, and slower rate of repolarization as compared with the somatic spike in *A*. *E* and *F*: superimposed simulations comparing the effects of various combinations of K^+ currents on the rate of dendritic spike repolarization. *E*: with no dendritic K^+ channels (trace 1), the dendritic spike has a long duration with the repolarizing phase interrupted by 2 small positive-going potentials reflecting the passive conduction of spikes generated at the soma (*). Trace 2 shows that $I_{Dr,d}$ can account for a large extent of the repolarizing phase of dendritic spikes. *F*: a comparison of the role for $I_{AptKv3.3}$ and $I_{Dr,d}$ in combination on dendritic spike repolarization. $I_{AptKv3.3}$ can account for a proportion of spike repolarization (trace 1 vs. 2), but the best fit is obtained when both $I_{Dr,d}$ and $I_{AptKv3.3}$ are present (trace 4). Removal of $I_{AptKv3.3}$ reveals a final role in adjusting both spike amplitude and repolarization (trace 3). Experimental methods for the recordings in *A* and *D* are as in Lemon and Turner (2000). Calibration bars in *B* and *E* also apply to *C* and *F*, respectively.

Na^+ and K^+ channels required to produce action potential waveforms that match in vitro recordings. Next we focus on the soma-dendritic interaction that gives rise to the DAP that drives burst discharge.

$I_{Na,s}$, $I_{Dr,s}$, and $I_{AptKv3.3}$: somatic spike

Figure 3*A* illustrates an action potential recorded in the soma of pyramidal cells in an in vitro slice preparation (see also Table 2 for quantitative comparison of model and experimental somatic action potential features). As we are interested in first modeling the somatic spike in the absence of backpropagating spikes, the recording in Fig. 3*A* was obtained after TTX had

TABLE 2. *Somatic action potential; model and experiment*

Action Potential Features	Pyramidal Cell Soma	Model Result
Half-width, ms	0.454 ± 0.159	0.585
Rise time, ms	0.299 ± 0.278	0.125
Decay time, ms	0.515 ± 0.3892	0.800
Amplitude, mV	80.9 ± 10.3	74.3

Comparison of model and experimental somatic spike features. All experimental results are taken from in vitro analysis presented in Berman and Maler (1998a). Values are means $\pm$ SD.

been locally applied to the entire dendritic tree. This effectively blocks all spike backpropagation and selectively removes the DAP at the soma (Lemon and Turner 2000). The somatic spike in pyramidal cells is of large amplitude (typically reaching 20-mV peak voltage) and very narrow half-width (width at half-maximal amplitude) of $\sim$0.45 ms (Table 2) (Berman and Maler 1998a; Turner et al. 1994). In the absence of a DAP, a fast afterhyperpolarization (fAHP) that follows the somatic spike is readily apparent (Fig. 3*A*). A slow Ca^{2+}-sensitive AHP (sAHP) follows the fAHP but does not contribute directly to the soma-dendritic interaction that underlies burst discharge (Lemon and Turner 2000).

ELL pyramidal cell somatic spikes are generated by TTX-sensitive Na^+ channels (Mathieson and Maler 1988; Turner et al. 1994), which are modeled here as a fast activating and inactivating current, $I_{Na,s}$. Rashid et al. (2001) established that Kv3 channels contribute to repolarizing the somatic spike in pyramidal cells. However, local blockade of somatic Kv3 channels using focal ejections of TEA in vitro only blocks a fraction of the total repolarization, indicating the additional involvement of other voltage-dependent K^+ channels. Pyramidal cells are known to express large conductance (BK) Ca^{2+}-activated K^+ channels in both somatic and dendritic mem-

branes (E. Morales and R. W. Turner, unpublished observations), but they do not appear to contribute to spike repolarization (Noonan et al. 2000; Rashid et al. 2001). A large fraction of the somatic spike repolarization is likely mediated by a small conductance K^+ channel (<10 pS) found with high prevalence in patch recordings (Morales and Turner, unpublished observations). Although the kinetic properties of this channel have not been established, whole cell currents in pyramidal cell somata indicate that it will have properties consistent with a fast activating and deactivating delayed rectifier-like (Dr) current, referred to here as $I_{Dr,s}$. We therefore model somatic spike depolarization and repolarization using a combination of $I_{Na,s}$, $I_{Dr,s}$, and $I_{AptKv3.3}$.

$I_{Na,s}$ and $I_{Dr,s}$ are confined to the somatic compartment, which includes both the initial segment and somatic membrane, and represents the site for Na^+ spike initiation in the cell (Turner et al. 1994). The activation (both $I_{Na,s}$ and $I_{Dr,s}$) and inactivation (only $I_{Na,s}$) steady-state conductance curve half voltages, $V_{1/2}$, and slopes, k, are similar to values used in previous compartmental models (Koch et al. 1995; Mainen et al. 1995; Rapp et al. 1996). Spike threshold occurs at $V_{thres} > -60$ mV, a value close to that reported for pyramidal cell spike threshold in vitro (Berman and Maler 1998a).

Previous compartmental models of mammalian neurons typically incorporate action potential half-widths of 1–2 ms (de Schutter and Bower 1994; Koch et al. 1995; Mainen et al. 1995; Rapp et al. 1996). Given the comparatively narrow half-width of ELL pyramidal cell spikes (Table 2), we choose relatively short $I_{Na,s}$ and $I_{Dr,s}$ time constants of activation and inactivation, τ_m and τ_h (Table 1), and $g_{max,Na,s}$ is set to 1.8 S/cm². To compensate the Na^+ conductance and achieve proper repolarization, $g_{max,Dr,s}$ is set to a value of 0.7 S/cm². We note that the model density of Na, s and Dr, s channels are comparable to that used in the spike initiation zone of other compartmental models (de Schutter and Bower 1994; Koch et al. 1995; Mainen et al. 1995; Rapp et al. 1996). Figure 3B shows somatic action potentials with $I_{Na,s}$ alone (trace 1) and both $I_{Na,s}$ and $I_{Dr,s}$ (trace 2) inserted in the model. The reduction in spike half-width and amplitude when $I_{Dr,s}$ is present allows the model somatic spike to better approximate experimental recordings (compare Fig. 3, A and B).

In considering the role of AptKv3.3 K^+ current, we find that AptKv3.3 channels alone could account for only a fraction of the total somatic spike repolarization. Figure 3C compares the somatic action potential with no $I_{Dr,s}$ or $I_{AptKv3.3}$-mediated repolarization (trace 1) to one with only $I_{AptKv3.3}$ current (trace 2). A reduction of spike width by $I_{AptKv3.3}$ during the initial falling phase of the action potential with a minimal reduction in peak voltage matches the results of earlier modeling studies that considered the role of Kv3.1 K^+ channels in spike repolarization (Perney and Kaczmarek 1997; Wang et al. 1998). As shown in Fig. 3C (trace 4), spike repolarization is most closely modeled when $I_{Dr,s}$ and $I_{AptKv3.3}$ are both present at the soma, with AptKv3.3 conductance set to 6.5 S/cm² (Rashid et al. 2001). Removing AptKv3.3 conductance slightly reduces the rate of spike repolarization without significantly affecting action potential amplitude. Such an effect on spike repolarization by AptKv3.3 is also consistent with pharmacological tests in vitro (Rashid et al. 2001).

$I_{Na,d}$, $I_{Dr,d}$, and $I_{AptKv3.3}$: dendritic spike

Many central neurons are known to be capable of actively backpropagating Na^+ spikes from the soma and over the majority of the dendritic tree (Stuart et al. 1997b; Turner et al. 1991, 1994; Williams and Stuart 1999; see Häusser et al. 2000 for review). Patch-clamp recordings in hippocampal pyramidal cells further indicate that Na^+ channels are distributed with a relatively uniform density over the entire dendritic tree (Magee and Johnston 1995); a distribution that has been used in other modeling studies (Mainen et al. 1995; Rapp et al. 1996). We have previously determined that Na^+ channel immunolabel in ELL pyramidal cells is uniformly distributed in the cell body region but exhibits a distinct punctate distribution over the proximal 200 μm of apical dendrites (Turner et al. 1994). This distribution correlated with the distance over which TTX-sensitive spike discharge was recorded, suggesting that the immunolabel correspond to Na^+ channels involved in spike generation. Electrophysiological recordings further established that Na^+ spikes are initiated in the somatic region but backpropagate over only ~200 μm of the dendritic tree that can extend as far as 800 μm (Maler 1979; Turner et al. 1994). In this respect, spike backpropagation in ELL pyramidal cell dendrites falls between the active conduction of Na^+ spikes seen over the entire axis of cortical neuron dendrites and the passive decay of Na^+ spikes seen over the proximal dendrites of cerebellar Purkinje cells (Häusser et al. 2000; Hoffman et al. 1997; Stuart and Häusser 1994; Stuart et al. 1997a).

Figure 3D shows an ELL pyramidal cell dendritic spike recorded ~150 μm from the soma. The dendritic spike half-width is substantially larger than that of the somatic spike, with the total duration approaching as much as 12 ms in recordings ~200 μm from the soma. Recordings in the slice preparation further indicate that even proximal dendritic spikes (50 μm) exhibit a sharp decrease in the rate of rise and rate of repolarization with respect to somatic spikes. This difference in rate of repolarization leads to a substantial delay in the peak latency of dendritic versus somatic spikes with a rapid increase in this difference beyond ~100 μm (Turner et al. 1994). Modeling this rapid change in spike characteristics in proximal dendrites requires a specific set of parameters for both dendritic Na^+ and K^+ conductances.

Given the immunocytochemical data (Turner et al. 1994), the distribution of dendritic Na^+ channels is confined to five punctate zones of 5 μm in length (200 μm² area) along the proximal apical dendrite that are assigned a high Na^+ channel density (Fig. 1). The distance between active dendritic zones also increases with distance from the soma. Specifically, active $I_{Na,d}$ zones 1–3 are separated by 15 μm of passive dendrite, while zones 3–5 are separated by 60 μm of passive dendrite. Lacking a cytochemical localization of $I_{Dr,d}$ K^+ channels in dendrites, we co-localized these channels to the five active dendritic zones. As stated in the preceding text, AptKv3.3 channels are incorporated over the entire soma-dendritic axis, although with varying levels of conductance for somatic, proximal apical dendritic, and distal apical and basal dendritic compartments.

We first attempted to equate the kinetic parameters of Na, d and Dr, d channels to those of somatic Na, s and Dr, s, respectively, but with reduced channel densities to produce a lower amplitude dendritic spike, as done in previous studies

(Mainen et al. 1995; Traub et al. 1994). However, this led to dendritic spikes with too short of a half-width and delay time to peak incompatible with intracellular dendritic recordings. A first attempt at correcting this discrepancy was raising the model axial resistance, thereby reducing the passive cable propagation of the spike along the dendrite. However, to obtain model agreement with experimental data, R_a had to be set outside acceptable norms by a factor of 10 (Mainen and Sejnowski 1998). This approach was problematic and hence abandoned.

Recently differences in ion channel kinetics have been observed for dendritic Na^+ and K^+ channels as compared with those at the soma, indicating precedence for applying differential kinetic properties to somatic versus dendritic ion channels (Colbert et al. 1997; Hoffman et al. 1997; Jung et al. 1997). Since a similar level of analysis is not yet available for ELL pyramidal cells, we explored a broad range of kinetic parameters describing both $I_{Na,d}$ and $I_{Dr,d}$. More successful modeling of experimental results is achieved by increasing the steady-state conductance curve slope, k, and time constant, τ, for both the activation and inactivation of $I_{Na,d}$ and $I_{Dr,d}$ as compared with their somatic counterparts. Simulations using only $I_{Na,d}$ and $I_{Dr,d}$ then begin to reproduce the delay in dendritic spike peak as well as the increase in spike half-width, the longer rate of rise, and the slower rate of repolarization when compared with the somatic spike (Fig. 3B). By comparison, modeling the dendritic spike with only $I_{Na,d}$ and $I_{AptKv3.3}$, does not achieve a sufficient rate of spike repolarization (Fig. 3F, trace 1 vs. 2). By combining $I_{Dr,d}$ with $I_{AptKv3.3}$ set to a density of 1 S/cm^2 in the proximal apical dendrite and a lower density of 0.5 S/cm^2 in other dendritic compartments a good fit to experimental data is obtained (cf. Fig. 3, D and F, trace 4).

Note that incorporation of $AptKv3.3$ current also reduces dendritic spike amplitude (Fig. 3F; trace 4). This result is consistent with experimental data indicating a slight increase in dendritic spike amplitude following local ejections of 1 mM TEA to block dendritic $AptKv3$ channels (Rashid et al. 2001).

Soma-dendritic interactions underlying the DAP

Figure 4 illustrates the effects of combining active somatic and dendritic compartments on spike waveforms. Previous intracellular recordings have indicated substantial differences in the duration and peak response of somatic versus dendritic spike waveforms (Fig. 4A). Both experimental recordings in Fig. 4A were obtained in intact slices with full backpropagation of spikes into dendrites. Under these conditions, the somatic spike is followed by a clear DAP that superimposes on the somatic fAHP (Fig. 4A). The DAP is due to the dendritic fast sodium currents, $I_{Na,d}$, which boost the backpropagating action potential to elevated voltages in the dendrite, and promotes return electrotonic current flow during the longer duration dendritic spike (Turner et al. 1994). When the model includes active spike discharge in both somatic and dendritic compartments, it successfully reproduces a DAP at the soma that is offset by the fAHP (Fig. 4B). If the g_{max} of all $I_{Na,d}$ currents is set to zero, in effect removing the active zones from the apical dendrite, the influence of the DAP at the soma is lost, uncovering a clear fAHP at the soma. Only a low-amplitude passive reflection of the somatic spike occurs in the apical dendrites (Fig. 4C), as recorded in vitro when TTX is focally applied to the dendrites to block active spike backpropagation (Turner et al. 1994).
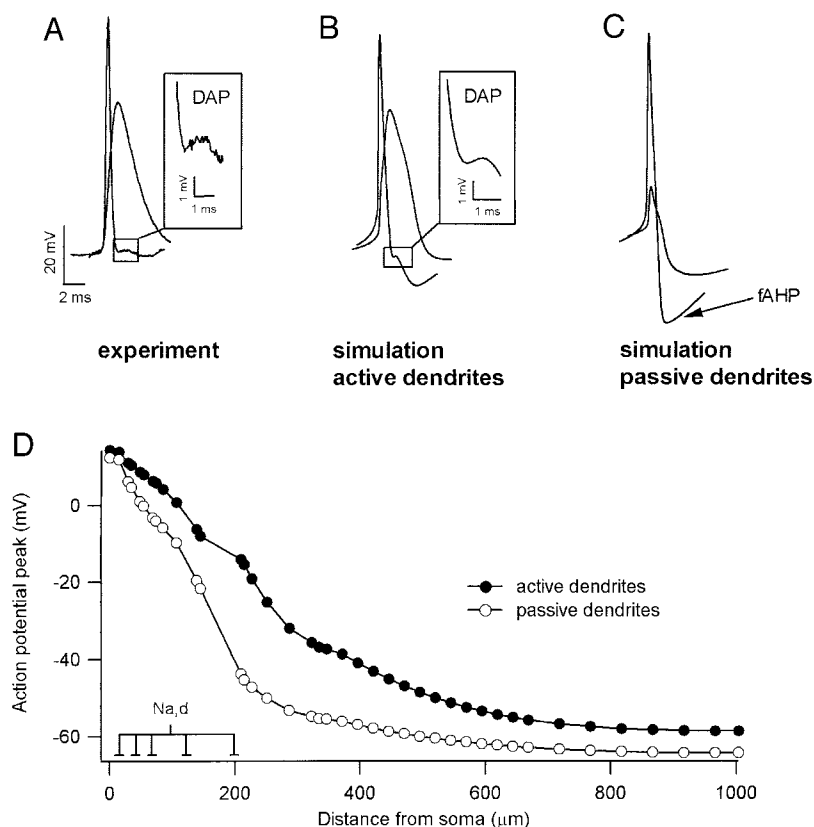

FIG. 4. Generation of a DAP through spike backpropagation. A: superimposed single spike discharge recorded in separate intracellular somatic and dendritic impalements (~200 μm from the soma), aligned temporally at the onset of spike discharge (Lemon and Turner 2000). The somatic DAP generated by the backpropagating spike is enlarged within the *inset*. The scale bars shown in A also apply to B and C. B: superimposed somatic and dendritic spike simulations (measured 200 μm from the soma) evoked by depolarizing somatic current injection. The somatic DAP is enlarged within the insert for comparison with A. Simulations in B and C also include I_{KA} and I_{KB} at the soma that underlies a late slow AHP (sAHP; not shown). C: superimposed model somatic and dendritic spike responses to somatic current injection with all $I_{Na,d}$ removed from the dendritic compartments. The somatic DAP is removed, uncovering the prominent fAHP. Note that only a small passive response is reflected into apical dendrites on the discharge of somatic spikes in the absence of $I_{Na,d}$. D: Plot of the peak voltage as a function of distance from the soma (0 μm) after discharging a somatic spike, with and without active dendritic $I_{Na,d}$ zones. The location of active sites in the proximal dendritic region are indicated *above* the abscissa. The slight deviation from expected passive decay in the proximal dendritic region is due to a reduction in the diameter of the model proximal dendritic shaft.

Spike backpropagation and refractory period

Figure 4*D* plots how the fitted kinetics of $I_{Na,d}$ and $I_{Dr,d}$ affect the backpropagation of action potentials initiated at the soma. Shown is the peak voltage of the response measured at a select number of compartments for both active propagation ($g_{max,Na,d} = 0.6$ S/cm^2) and passive electronic conduction ($g_{max,Na,d} = 0$ S/cm^2) in the dendritic compartments. In the proximal apical dendrite (<200 μm), the five active $I_{Na,d}$ sites incorporated into the model boost the peak of the backpropagating action potential over that measured during passive conduction. In the mid-distal dendrite (>200 μm), the peak voltage decays exponentially in both cases because no active inward currents are believed to boost the voltage beyond this distance (Turner et al. 1994). This decrease in spike amplitude near 200 μm also qualitatively mimics the properties of backpropagating spikes as measured through laminar profile field potential analysis (Turner et al. 1994).

To test the accuracy of fit of channel parameters for $I_{Na,s}$, $I_{Na,d}$, $I_{Dr,s}$, and $I_{Dr,d}$, we measure the refractory period of both somatic and dendritic spikes (Fig. 5, *A* and *B*). The simulation protocol is equivalent to the condition-test (C-T) interval experiment used by Lemon and Turner (2000). In the model, this consists of first injecting a brief somatic current pulse sufficient to induce a single somatic spike that backpropagates into the dendrites. A second identical current pulse is then applied at a variable time interval following the first pulse to identify relative and absolute refractory periods. At sufficiently long test intervals (Fig. 5, *A* and *B*, 8 ms) the second pulse evokes full somatic and dendritic spikes, both identical to the condition responses. At the soma, a reduction in the C-T interval to $\sim$4 ms results in a select blockade of the DAP without significant effect on the somatic spike (Fig. 5*A*). Somatic spike amplitude remains essentially stable for C-T intervals above 2.5 ms, although C-T intervals below this slightly reduce spike amplitude, given that $I_{Na,s}$ has not completely recovered from inactivation. An absolute somatic refractory period is evident at a C-T interval of 1.5 ms (Fig. 5*A*). The effects of a similar series of C-T intervals monitored 200 μm from the soma reveals a relative refractory period for dendritic spikes between 4 and 6 ms, as reflected by a gradual decline in spike amplitude. This reduction in amplitude ends at C-T intervals between 2.0 and 3.0 ms (Fig. 5*B*), with subsequent failure of the small potential evoked at C-T intervals of $\sim$1.5 ms.

Each of these properties qualitatively match experimental results in pyramidal cells of an absolute somatic refractory period at $\sim$2 ms, a relative dendritic refractory period between 5 and 7 ms and an absolute dendritic refractory period between 3 and 4 ms (Lemon and Turner 2000). Furthermore a selective block of the somatic DAP over the same range of C-T intervals that reduce dendritic spike amplitude is also a characteristic observed in intact pyramidal cells (Turner et al. 1994).

I_{NaP}—determining RMP, nonlinear EPSP boosting, and latency to first spike shifts

A TTX-sensitive and persistent Na$^+$ current (I_{NaP}) (French et al. 1990) has been recorded at both the somatic and dendritic level of ELL pyramidal cells (Berman et al. 2001; Turner et al. 1994). Blocking this current with focal ejections of TTX in vitro results in a clear hyperpolarizing shift in cell resting
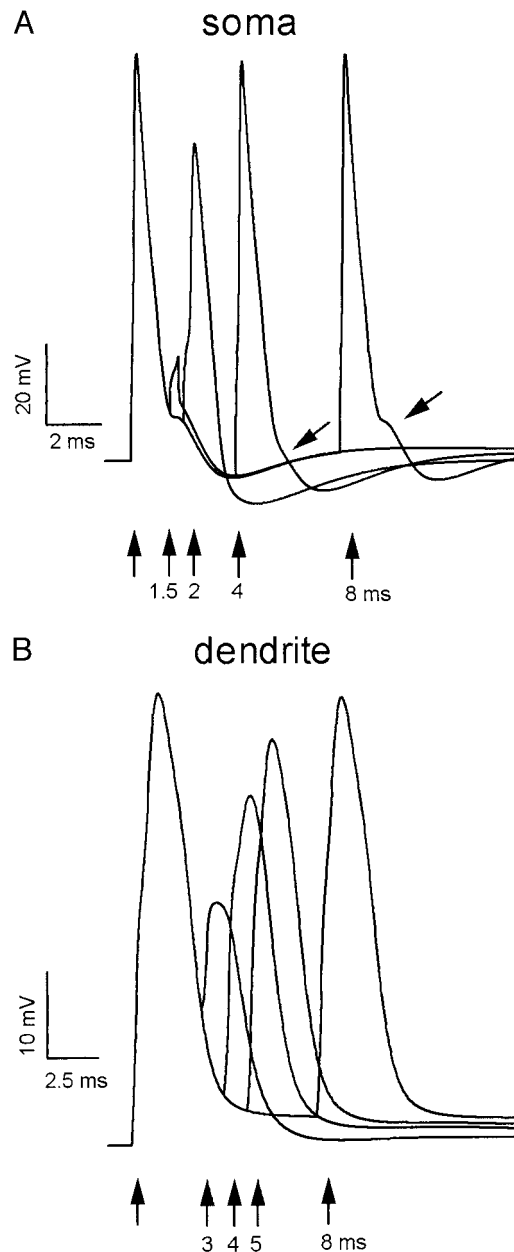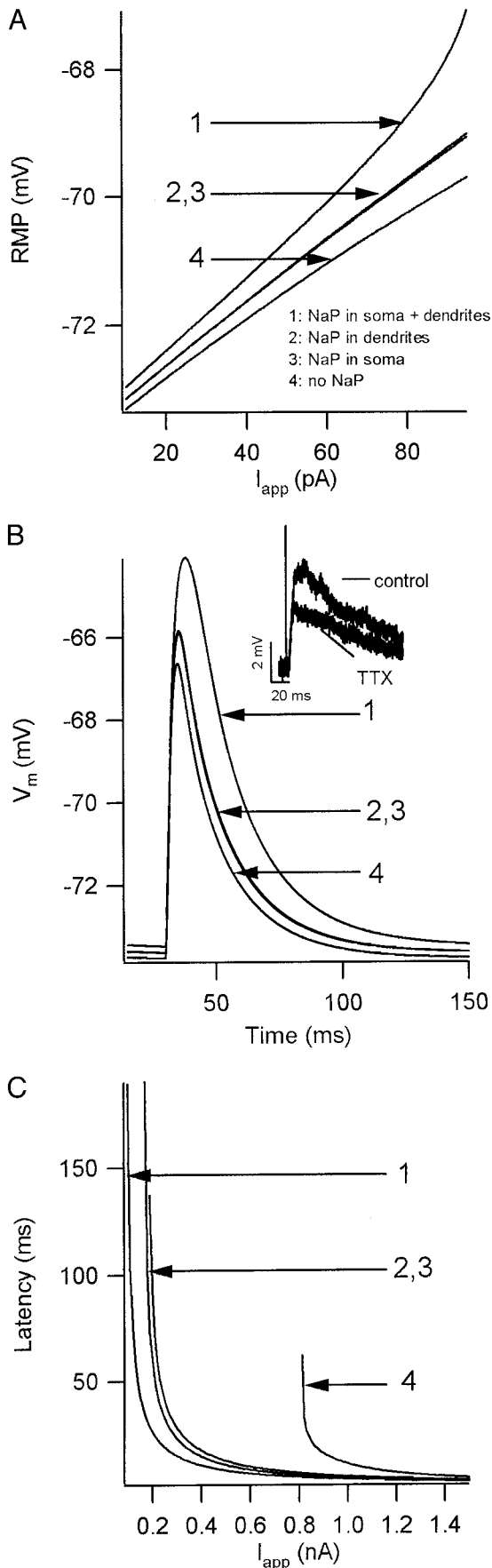

FIG. 5. Refractory period of model somatic and dendritic spikes. Spike discharge was evoked with a short-duration depolarization at the soma and a condition-test (C-T) pulse pair presented at varying intervals to determine if the model reproduced the observed differential refractory period between somatic and dendritic regions of pyramidal cells. *A*: several superimposed C-T stimulus pairs at the soma. The C-T interval is indicated below the traces (arrows). The absolute refractory period of the model somatic spike occurs at 1.5 ms. Note that the somatic DAP is also selectively blocked at a C-T interval of 4 ms (slanted arrows) with no significant change in the somatic spike. *B*: superimposed C-T stimuli monitored at 200 μm in the dendrite. The dendritic spike exhibits a relative refractory period beginning at $\sim$6 ms as shown by a decline in spike amplitude at progressively shorter C-T intervals. An absolute refractory period at 3 ms is indicated by the final presence of only a passively reflected response associated with the somatic spike. Each of these properties accurately reflect the conditions found in ELL pyramidal cells in vitro.

membrane potential (RMP) and an increase in the latency to discharge a spike at the soma (Turner et al. 1994). There is also a prominent voltage-dependent late component to the dendritic and somatic excitatory postsynaptic potential (EPSP) evoked by stimulation of descending tractus stratum fibrosum (tSF)

inputs that terminate in the proximal dendritic region (Berman and Maler 1998c; Berman et al. 1997). Recent work indicates that focal ejection of TTX at the soma selectively blocks this late component of the tSF-evoked EPSP (Berman et al. 2001). Each of these results identifies an important contribution by I_{NaP} in determining the resting membrane potential (RMP) of the cell, in boosting the tSF synaptic depolarization, and in setting the latency to spike discharge. We determine the model NaP channel parameters through a detailed match to these constraints.

NaP channels are modeled in both the soma and proximal apical dendrite as suggested by experimental and modeling studies of ELL pyramidal cells (Fig. 1) (Berman and Maler 1998c; Turner et al. 1994). In the absence of definitive knowledge of the distribution of dendritic NaP channels, a uniform distribution of NaP channels over the entire proximal apical dendrite is chosen. Local TTX applications in vitro produce quantitatively similar shifts in RMP at both the somatic and dendritic level of pyramidal cells (Turner et al. 1994). We hence choose a relative factor of 3.5 for the ratio of total somatic/dendritic NaP channel density to account for the greater proximal apical dendritic surface area. This produces approximately equal net I_{NaP} current from both soma and dendrite in response to similar depolarizations.

To set the NaP channel activation parameters, $V_{1/2}$ and k, we consider its effects on the model cell RMP. To do so, we apply a small constant depolarizing somatic current injection to the model ($I_{app} < 100$ pA), which is insufficient to cause spiking. After a transient period of depolarization, the model membrane voltage settles to a steady-state value, which we label as the "effective" RMP. The shape of the increase in RMP as I_{app} increases will be determined by the specific NaP distribution. Figure 6A plots this final equilibrium somatic voltage ($t > 200$ ms) as a function of I_{app} with NaP present in various compartments (see figure legend for description). For small currents ($I_{app} < 50$ pA), the rise in RMP is linear (Ohm's law) because at these potentials ($V_m < -70$ mV) NaP is not significantly activated. However, for larger applied currents ($I_{app} > 60$ pA) yielding higher RMP values ($V_m > -70$ mV), a significant nonlinear RMP increase occurs when NaP is present (trace 1, Fig. 6A). This effect requires a steep subthreshold voltage dependency of activation that forces the half activation of I_{NaP}, $V_{1/2,m,NaP}$, to be set to -58.5 mV and the activation slope parameter, $k_{m,NaP}$, to be low, 6 mV. This agrees with the

FIG. 6. The effects of somatic or dendritic I_{NaP} on resting membrane potential (RMP), excitatory postsynaptic potential (EPSP) amplitude, and spike latency. A: RMP in the model cell plotted as a function of a series of subthreshold depolarizing current injections (I_{app}) 200 ms after the onset of the depolarization, at which point $dV_{soma}/dt \approx 0$. Several superimposed plots are shown labeled according to the model conditions: control (all parameters are as given in Table 1), somatic $g_{NaP} = 0$, dendritic $g_{NaP} = 0$, and both somatic and dendritic $g_{NaP} = 0$ (see figure legend). Note the linear displacement of potential with no I_{NaP} present (trace 4), but a nonlinear increase in membrane voltage with current injection when I_{NaP} is present in both somatic and proximal dendritic compartments (trace 1). B: model somatic responses to an evoked EPSP in the proximal dendritic region (200 μm from soma; alpha function, $\tau = 1.5$ ms, $g_{max} = 16$ nA) for the NaP conditions as labeled in A. Inset: pyramidal cell somatic EPSPs evoked by tractus stratum fibrosum (tSF) inputs to the proximal dendrites before and after focal somatic TTX ejection to block I_{NaP} (Berman et al. 2001). C: latency to 1st spike is plotted as a function of suprathreshold depolarizations for the NaP conditions shown in A. Trace 1 best approximates previous experimental latency measurements from ELL pyramidal cells (Berman and Maler 1998a).

experimental effects of TTX application on pyramidal cell RMP in vitro (Berman and Maler 1998c; Turner et al. 1994) and with experimentally determined $V_{1/2}$ (-56.92 mV) and k (9.09) voltages for NaP in rat and cat thalamocortical neurons (Parri and Crunelli 1998). The quantitative agreement with experiment is achieved by adjusting $g_{max,NaP}$. However, since f-I characteristics (see Fig. 8) are compromised with a significant modification of $g_{max,NaP}$, the fit is balanced to produce a realistic RMP, and proper f-I relationship for the model cell.

As illustrated in Fig. 6A, restricting the NaP distribution to either somatic or dendritic membranes (traces 2 and 3) reveals the nonlinear effect of NaP density in determining the RMP (for $I_{app} > 80$ pA the difference between traces 1 and 4 is larger than the sum of the differences between traces 2 and 3 with 4). The nonlinear effect will be treated when we analyze the role of NaP in EPSP boosting (see following text). The near exact quantitative agreement of traces 2 and 3 in Fig. 6A indicate that the effect of NaP on the RMP is not site-specific between soma and proximal dendrite. This is expected since the net NaP currents of both somatic and dendritic membranes are set to be equal (see preceding text). The parameters that model the steady-state characterization of the NaP, $V_{1/2,m,NaP}$, and $k_{m,NaP}$, are now set; however, the dynamics of the I_{NaP} current, determined by $\tau_{m,NaP}$, remains to be addressed.

I_{NaP} currents have been shown to boost the amplitude of subthreshold EPSPs in cortical pyramidal cells (Andreasen and Lambert 1999; Lipowsky et al. 1996; Schwindt and Crill 1995; Stafstrom et al. 1985; Stuart and Sakmann 1995); there is recent evidence in ELL pyramidal cells for a similar effect (Berman and Maler 1998c; Berman et al. 2001). To set the time constant of NaP activation, $\tau_{m,NaP}$, we consider the EPSP boosting properties of the model I_{NaP}. The *inset* in Fig. 6B shows somatic recordings of a distally evoked EPSP under control and somatic TTX conditions. The boost provided by TTX-sensitive currents begins with the fast rising phase of the EPSP, suggesting that NaP channels activate quickly (Fig. 6B; compare the *inset* control trace to the TTX trace). To match the data, the model $\tau_{m,NaP}$ is set to a small value ($\tau = 0.3$ ms). This fast activation coincides with the treatment of I_{NaP} in other ionic models (Lipowsky et al. 1996; Wang 1999). Figure 6B shows the model somatic voltage response due to dendritic EPSP activation under the same various NaP distributions considered in Fig. 6A. The EPSP boost observed with all distributions shows that the subthreshold boost of the EPSP by I_{NaP} is substantial and that indeed the boost begins with the rising edge of the potential, thereby matching experimental data.

The nonlinear nature of I_{NaP} boosting of EPSPs is apparent in Fig. 6B when we compare EPSP amplitudes when NaP is present in both the somatic and proximal apical dendritic compartments (trace 1) to NaP distributions in only in the somatic (trace 2) or dendritic (trace 3) compartments. Figure 6B shows approximately a 3-mV boost of the model EPSP amplitude when comparing the control case to complete NaP removal (trace 1 as compared with 4). However, with only somatic or dendritic NaP distribution (trace 2 or 3), a boost of <1 mV at the peak of the EPSP is observed. A linear increase in the degree of EPSP enhancement would require that the effects of traces 2 and 3 summate algebraically to produce trace 1. The nonlinear boosting is a result of the steep sigmoidal voltage activation of NaP (plot not shown).

It has been experimentally shown in thalamocortical neurons that I_{NaP} activation reduces the latency to spike in response to depolarizing current (Parri and Crunelli 1998). We hence further test the fit of NaP parameters by considering the model cell's latency to discharge a spike on membrane depolarization. Figure 6C plots the model latency to first spike as a function of applied somatic suprathreshold depolarizing current under all four NaP conditions described in Fig. 6 (A and B). All traces show that just above the rheobase current (minimum current required to induce spiking) the latency to first spike is long, yet as the input current is increased, the latency decays to shorter values. Comparing the various NaP conditions reveals that increasing I_{NaP} reduces the rheobase current of the cell, with a full 0.71-nA shift occurring between the condition in which all somatic and dendritic NaP removed (trace 4) as compared with the condition in which I_{NaP} is distributed over the both somatic and dendritic membranes (trace 1). As a result of the rheobase shift, Fig. 6C shows the latency to first spike at $I_{app} = 0.81$ nA with all NaP removed to be 62.4 ms as compared with the control latency of 4.3 ms at the same current.

Figure 6C also indicates that the nonlinear effects of I_{NaP} already seen on the RMP and EPSP amplitude are even more dramatic on both the rheobase current and latency shift. Partial removal of NaP (traces 2 and 3) only shifts the rheobase and the latency to first spike by slight amounts from the control case (trace 1) when compared with the dramatic shifts observed with a block of both somatic and dendritic I_{NaP} (trace 4). The quantitative agreement between latency shifts observed when either somatic or dendritic NaP are removed shows that there is no spatial differences of NaP effects on rheobase current or latency as expected by the spatially balanced net ionic current.

Finally, we compare the model spike latency characteristics with experimental measurements from ELL pyramidal cell latency to spike (Berman and Maler 1998b). In ELL pyramidal cells, the transition from long to short latencies to spike does indeed occur over a small depolarizing current interval (~ 0.1 nA), as in the model control case (trace 1, Fig. 6C). The model results show a power law decay (spike latency $\sim 1/\sqrt{I_{app} - I_{rheobase}}$). However, experimental work indicates a step decline from long latencies (>20 ms) to a constant latency (~ 4 ms) for large depolarization (Berman and Maler 1998b). This could not be fit with a power law as in the model results. The model latency decay occurred with all I_{NaP} parameter sets explored; however, the given fitted parameters (Table 1) produced the best approximation to experimental latency shifts. The discrepancy between the experimental and model latency decay is presently unexplained.

I_A—latency to first spike from hyperpolarized potentials

Previous studies of ELL pyramidal cell electrophysiology (Berman and Maler 1998b; Mathieson and Maler 1988) have suggested the existence of a transient outward current similar to I_A (Connor and Stevens 1971). Both studies observed an increase in spike latency if a depolarization was preceded by membrane hyperpolarization, an effect previously attributed to the activity of an I_A current (Connor and Stevens 1971; McCormick 1991). At this time, patch-clamp recordings have not conclusively shown the possible contribution of an I_A current at the somatic or dendritic level of pyramidal cells (Turner, unpublished observations). Our attempts to simulate the exper-

iments performed in Mathieson and Maler (1988) now show that to reproduce the observed effects of membrane potential on the latency to spike discharge, a low density of I_A-like K$^+$ current must be introduced into the model cell.

Because patch-clamp recordings in pyramidal cells have not yet isolated transiently activating and inactivating channels consistent with a traditional A-type K$^+$ current, the choice of channel distribution over the model cell must be postulated. A previous compartmental model has shown that altering the distribution of I_A channels over a cell gives only small deviations in observed I_A character, with the exception of cells with large axial resistance (~2,000 Ωcm) (Sanchez et al. 1998). Our model neuron axial resistance (250 Ωcm) is much lower, and hence any chosen channel distribution should not significantly affect cell output. Considering this result, we distribute I_A uniformly over the whole cell (Fig. 1).

The half voltages for the steady-state conductance curves for I_A currents are set to $V_{1/2,m,A} = -75$ mV and $V_{1/2,h,A} = -85$ mV and the curve slope factors to $k_{m,A} = 4$ mV and $k_{h,A} = -2$ mV. Other models of I_A (Huguenard and McCormick 1992; Johnston and Miao-Sin Wu 1997; Sanchez et al. 1998) show I_A window currents at more depolarized levels ranging over a larger voltage interval. However, in the absence of definitive I_A characterization in ELL pyramidal cells, we choose to fit the activation/inactivation parameters to ensure that I_A does not affect the model RMP yet that inactivation could be removed

with moderate hyperpolarization (in correspondence with the results of Mathieson and Maler 1988). $\tau_{m,A}$ is set to 10 ms to have sufficiently rapid A-type K$^+$ channel activation (Johnston and Miao-Sin Wu 1997). However, the time constant of I_A inactivation, $\tau_{h,A}$, is chosen to be 100 ms to produce an appropriate latency to first spike and a subsequent transient increase in spike frequency over the first 200 ms (Doiron et al. 2001).

Figure 7A shows the model cell response without I_A present ($g_{max,IA} = 0$) to a depolarizing somatic current injection of 0.6 nA. The model cell is at a resting potential of -73 mV prior to the stimulus. A repetitive firing pattern results with a latency to first spike of 6.05 ms (stimulus onset is at $t = 0$) and ISI of 9.5 ms. Figure 7B repeats this simulation but with a 50-ms prestimulus hyperpolarization of -11 mV induced via -0.2-nA current injection. Again, repetitive firing occurs, yet with a slightly longer latency to first spike of 12.1 ms followed by a repeating ISI of ~9.5 ms. These results qualitatively match those obtained by Mathieson and Maler (1988) when 1 mM 4-aminopyridine (4-AP, a known I_A channel blocker) was bath applied to ELL pyramidal cells in vitro. However, under control conditions, a substantially longer latency to first spike was observed in ELL recordings when a prestimulus hyperpolarization preceded depolarization (Mathieson and Maler 1988). Furthermore when depolarizing current is applied from a hyperpolarized level, the first ISI is long and then subsequent ISIs
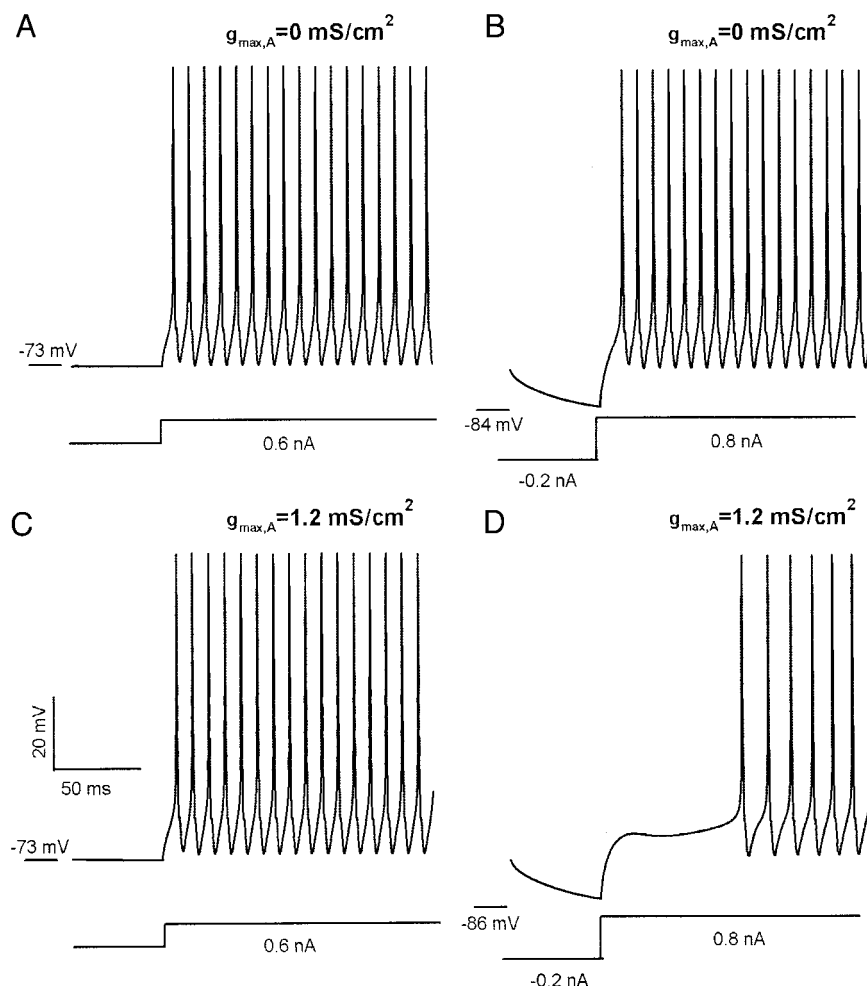

FIG. 7. The effects of I_A on latency to spike discharge. All panels show the model response to a particular applied current protocol as indicated below each simulation. Each panel marks the I_A channel conductance used in the simulation and the value of the membrane potential at the time of depolarization. A and B: core model response in the absence of I_A to equivalent depolarizations from a resting potential of -73 mV (A) or following a prestimulus hyperpolarization to -84 mV (B). C and D: the model response to a similar current injection protocol when I_A is inserted into the model. At -73 mV resting potential (C) I_A is inactivated, leading to an equivalent response to that shown in A. Note that depolarizing the cell following a prestimulus hyperpolarization (D) results in a substantially longer latency to spike when I_A is present (cf. B and D). The set of calibration bars shown in C applies to all panels.

slowly shorten (an increase in cell firing rate) in the first 200 ms of the stimulus, presumably due to I_A inactivation.

Figure 7, *C* and *D,* illustrates simulation protocols identical to those shown in *A* and *B,* respectively, yet with I_A channels distributed across the model cell. $g_{max,IA}$ is fit to match the experimental findings of Matheison and Maler (1988) with a final assigned value of $g_{max,IA} = 1.2$ mS/cm^2. At a resting potential of -73 mV, I_A is substantially inactivated so that depolarizing the somatic compartment via a 0.6-nA current injection results in a latency to first spike and subsequent ISI shift that is nearly identical to the results obtained when I_A is not incorporated into the model (cf. Fig. 7, *A* and *C*). However, with a prestimulus hyperpolarization, the same net current injection produces a latency to first spike of 78.5 ms, an increase of 66.3 ms as compared with spike discharge without a prestimulus hyperpolarization (Fig. 7*D*). In addition, in the presence of I_A the ISI begins at 14.4 ms and reduces to 10 ms after 200 ms of depolarization, successfully reproducing the gradual increase in spike frequency observed in pyramidal cells (not shown). Smaller depolarizations ($I_{app} < 0.6$ nA) following equivalent prestimulus hyperpolarizations ($I_{app} = -0.2$ nA) induce larger differences in latencies to first spike for cases without I_A. Similarly, larger depolarizations ($I_{app} > 0.6$ nA) give smaller latency shifts. These results are also qualitatively similar to the ELL experimental results of Matheison and Maler (1988).

Since $g_{max,x}$ represents the maximal channel conductance of current I_x in the compartment of interest, it provides an indirect value for the expected channel density of the channel in that compartment. It is therefore interesting to note that comparing the model currents $I_{AptKv3.3}$ to I_A shows that $g_{max,AptKv3.3}$ is three orders of magnitude larger than $g_{max,A}$ when spike discharge properties are properly reproduced. If this is an accurate representation of the situation in pyramidal cells, the high-density of *Apt*Kv3.3 could have masked evidence of an I_A in patch-clamp recordings.

I_{KA}, I_{KB}—somatic K$^+$ currents

Somatic K$^+$ currents in ELL pyramidal cells have only recently been subjected to voltage-clamp analysis and cannot be fitted as stringently as currents discussed in previous sections. However, without a proper treatment of somatic K$^+$, both the model *f-I* relationship and spike frequency adaptation disagree with experimental results. In this section, we introduce two somatic K$^+$ currents, I_{KA} and I_{KB}, to improve model performance in these areas.

Whole cell recordings in ELL pyramidal cell somata indicate a prominent expression of Ca^{2+}-dependent large conductance (BK) K$^+$ channels (Morales and Turner, unpublished observations). The effect of these channels is modeled by a voltage-dependent current, I_{KA}, because of the uncertainties on the location and magnitude of Ca^{2+} influx in pyramidal cells. The dynamics is similar to that of $I_{AptKv3.3}$, given the fast rate of BK activation and deactivation in ELL pyramidal cells (Morales and Turner, unpublished observations). Specifically, a fast activation time constant (small $\tau_{m,KA}$) is chosen for I_{KA} dynamics, and the current is set to be high threshold in its initial activation (small $k_{m,KA}$ and depolarized $V_{1/2,m,KA}$, see Table 1).

Whole cell recordings reveal that iberiotoxin-sensitive BK K$^+$ channels contribute $\sim$75% of the somatic K$^+$ current

(Morales and Turner, unpublished observations). Consequently the g_{max} of I_{KA} is adjusted to first establish the BK simulated current to a level approximately triple that of somatic $I_{AptKV3.3}$ at voltages >0 mV (results not shown). Because of its fast activation and the lack of inactivation, I_{KA} overlaps the sAHP following a somatic spike and hence significantly affects the model *f-I* relationship. Thus in addition, the channel density, $g_{max,KA}$, is set so that *f-I* characteristics of the model more closely approximate ELL pyramidal cells (see Fig. 8). The *f-I* curves show a rheobase current of 0.1 nA with a saturating rise in spike frequency as current increases. This is equivalent to measured *f-I* curves from ELL pyramidal cells in control situations (Berman and Maler 1998b; Lemon and Turner 2000).

Spike frequency adaptation during long current pulses (Matheison and Maler 1988) has been reported in some ELL pyramidal cells, although it is typically not prominent. The original version of our model incorporated a slow, noninactivating K$^+$ current termed I_{KB} to provide correct frequency adaptation under constant depolarizing current (Doiron et al. 2001). The kinetic parameters of this current are not modified from the original model, where comparisons between experimental and model frequency adaptation are presented.

In summary, the core pyramidal cell model includes 10 ionic currents, each described by separate Hodgkin/Huxley dynamics. Model *Apt*Kv3.3 currents match HEK cell experiments that isolate and describe properties of this current. The model cell gives the correct shape and refractory properties for both somatic and dendritic spikes and the generation of a DAP at the soma by the backpropagating spike. The model somatic and dendritic NaP channels produce the correct shifts in RMP, boosting of EPSPs, and reduction in spike latencies from rest, as observed in experimental recordings in vitro. A-type K$^+$ channels are included so as to give correct latency to spike from hyperpolarized potentials. Finally, the model shows correct passive and *f-I* characteristics as determined from intracellular recordings.
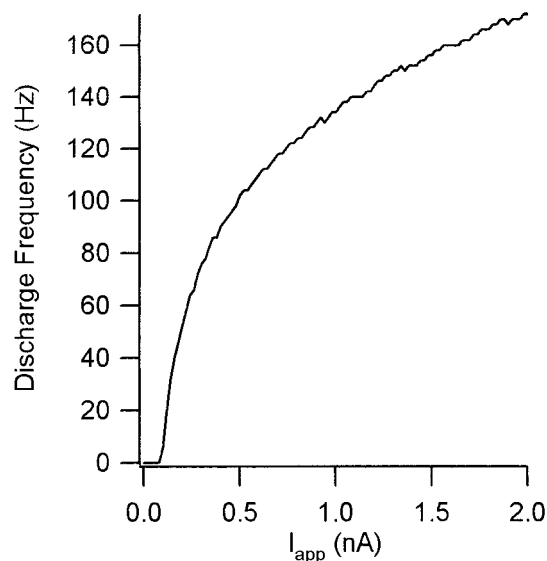

FIG. 8.   Spike frequency-current (*f-I*) characteristic of the model. The frequency of spike discharge of the model for a given bias current I_{app} applied to the soma is measured as the mean discharge rate over 500 ms, after a 100-ms transient period. I_{app} is incremented in steps of 0.02 nA.

ELL pyramidal cell bursting

Figure 9*A* shows the model's repetitive discharge properties (nonburst activity) in response to depolarizing somatic current injection. However, the lack of a transition to γ-burst discharge suggests that there are missing elements in the model. We should note that electrophysiological work to date has reported no evidence for a low-threshold "T"-type Ca^{2+} current or I_h in ELL pyramidal cells, two currents known to underlie burst discharge in many cell types (Huguenard 1996; Pape 1996). Rather, burst discharge in ELL pyramidal cells comes about through a progressive shift in the interaction between soma and dendrite during repetitive discharge (Lemon and Turner 2000). In the following sections, we alter the kinetic properties of specific ion channels to test their ability to generate burst discharge in the core model. We first introduce a well-studied bursting mechanism involving slow activating K^+ channels (Chay and Keizer 1983) in the hopes of achieving bursting.

Burst discharge in the model does occur but fails to qualitatively reproduce several burst properties in somatic and dendritic recordings of ELL pyramidal neurons. We then insert various potential burst mechanisms into the ionic description of the model. It will be shown that a slow, cumulative, inactivation of a dendritic K^+ current coupled with the longer refractory period of the dendritic spike as compared to the somatic spike is required to reproduce ELL pyramidal cell γ-bursting.

Standard burst mechanism: slow activating K^+ current

Reduced dynamical burst models show a characteristic ability to switch between stable oscillatory discharge (burst) and quiescent rest voltage (inter-burst) (see Izhikevich 2000; Rinzel 1987; Wang and Rinzel 1995; for a review of dynamical bursting models). What is required to switch between these states is a slow dynamical variable. In most previous compartmental models of intrinsic bursting, this slow variable is a
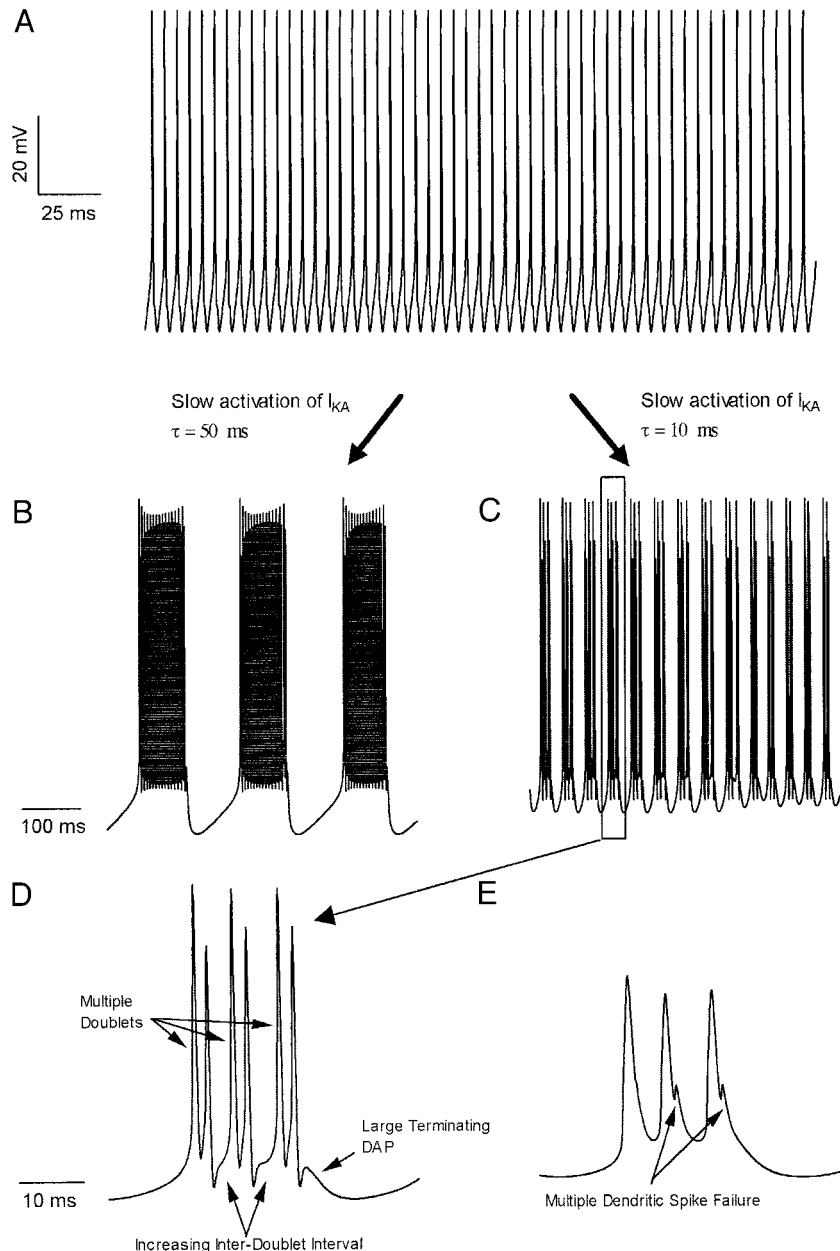

FIG. 9. The influence of a slowly activating K^+ current (I_{KA}) does not reproduce burst discharge observed in ELL pyramidal cells. All simulations have a tonic depolarizing current of 0.6 nA applied to the somatic compartment. *A*: repetitive firing of the core model. *B*: when the activation time constant of I_{KA}, τ_{KA}, is set to 50 ms, a very-low-frequency (~6 Hz) burst pattern results. *C*: when the activation time constant of I_{KA} is set to 10 ms, a higher frequency (~30 Hz) burst pattern results. *D*: an expanded view of a single burst from the somatic spike train shown in *C*. Although a higher frequency of spike bursts is generated with τ_{KA} = 10 ms, the existence of a repeating series of spike doublets, a progressively increasing inter-doublet interval, and a large terminating DAP all disagree with experimentally observed ELL bursts. *E*: the dendritic response (200 μm) during the single somatic spike burst shown in *D*. Multiple dendritic spike failures (arrows) and the lack of a slow summating depolarization during the spike train disagree with experimental observations of pyramidal cells in vitro.

Ca^{2+} and/or voltage-dependent K^+ channel, $K_{(Ca)}$ (Chay and Keizer 1983; Mainen and Sejnowski 1996; Pinsky and Rinzel 1994; Rhodes and Gray 1994; Traub et al. 1994; Wang 1999; to name but a few). The mechanism involves increases in intracellular Ca^{2+} due to repetitive firing. This causes a slow activation of $K_{(Ca)}$, thereby hyperpolarizing the cell. The hyperpolarization by $K_{(Ca)}$ first acts as a voltage shunt, increasing the ISIs at the tail of a burst. When $K_{(Ca)}$ is sufficiently activated, spike discharge stops completely, and the burst terminates. At hyperpolarized levels, $K_{(Ca)}$ deactivates, and spiking (bursting) may once again occur, given sufficient depolarization. This gives a characteristic burst pattern, with an increasing ISI during the length of the burst. This pattern has been observed in both experiment (Gray and McCormick 1996) and models that use $K_{(Ca)}$ (Wang 1999).

Burst discharge in ELL pyramidal cells is insensitive to the Ca^{2+} channel blocker Cd^{2+} (Rashid et al. 2001), and hence $K_{(Ca)}$ is presumably not implicated in the burst mechanism. Yet a slow, increasing K^+ current that terminates the burst is still a potential mechanism. Rather than hypothesize a new ionic K^+ channel, we modify the existing somatic I_{KA} to produce the desired effects. Specifically, Fig. 9 shows the model somatic voltage under constant somatic current injection after the activation time constant $\tau_{m,KA}$ is increased from 1 ms (Fig. 9A) to 50 ms (Fig. 9B). Bursting occurs, yet with a burst frequency of ~5 Hz, whereas pyramidal neurons exhibit typical burst frequencies in the γ range (20–80 Hz) (Lemon and Turner 2000). To rectify the discrepancy, $\tau_{m,KA}$ is reduced to 10 ms with the corresponding spike train shown in Fig. 9C. The burst frequency now approaches experimental values, but the spike pattern within a burst disagrees with experimental data. We elaborate on the discrepancies in the following text.

Figure 9 (D and E) illustrates the somatic and dendritic (200 μm) responses during a single burst from the train shown in Fig. 9C. During a burst, the model somatic voltage shows the existence of *multiple* spike doublets (2 spikes at >200-Hz frequency), while the dendritic voltage shows *multiple* spike failures (Fig. 9, D and E). Both somatic and dendritic bursts show no growing depolarization during the burst as evident from the lack of both an increasing DAP at the soma and spike summation in the dendrite. Dendritic spike broadening is not observed during the length of a burst, and the somatic spike train is followed by a large DAP that fails to elicit a spike due to a large KA conductance at the end of the burst. Finally, Fig. 9D shows an *increasing* inter-doublet interval during a burst. This result is similar to other bursting models incorporating a slow activating K^+ current (Rhodes and Gray 1994; Wang 1999) but does not match the properties of burst discharge in ELL pyramidal cells (Lemon and Turner 2000). Therefore these discrepancies indicate that a slow activating K^+ current is inadequate to model the burst discharge that incorporates conditional backpropagation in ELL pyramidal neurons.

ELL burst mechanism

To produce an output that more closely simulates pyramidal cell burst discharge, we concentrate on methods in which a decreasing ISI pattern during a burst can be realized in the model. The duration of an ISI is determined by the amount of somatic depolarization that produces the next spike in a spike train. Hence changes in ISIs must be linked to changes in the amount of depolarization during a spike train. In the present study, somatic depolarization is determined from two sources: a constant applied current I_{app} and a dendritic component activated by spike backpropagation that generates the DAP. Because I_{app} is constant, the ISI decrease observed during a burst should be correlated with increases in the DAP as shown by Lemon and Turner (2000). Four possible alternatives for DAP increase present themselves. First, cumulative inactivation of dendritic fast Na^+ current could broaden dendritic spikes indirectly by diminishing the activation of dendritic repolarizing currents ($I_{Dr,d}$ and $I_{AptKv3.3}$). The broadening of the dendritic spike could lead to DAP growth at the soma. Second, a slowly activating inward current could increase the dendritic depolarization during repetitive discharge and hence augment the somatic DAP. Third, a cumulative inactivation of a dendritic K^+ current involved in dendritic spike repolarization would increase dendritic spike duration during a burst and increase the DAP. The fourth potential mechanism is a cumulative decrease in K^+ currents underlying AHPs at the soma that would allow the DAP to become progressively more effective in depolarizing somatic membrane. However, this mechanism has been ruled out because somatic AHPs are entirely stable in amplitude at the frequencies of spike discharge encountered during burst discharge (Lemon and Turner 2000). We consider each of the remaining alternatives in the following text.

Slow inactivation of dendritic Na^+ channels

Patch-clamp recordings in hippocampal pyramidal cells have shown that the amplitude of dendritic spikes are reduced substantially during repetitive discharge (Colbert et al. 1997; Golding and Spruston 1998; Jung et al. 1997; Mickus et al. 1999). The reduction in dendritic spike amplitude saturates during long stimulus trains, giving a final steady-state potential height. Jung et al. (1997) and Colbert et al. (1997) have identified the cause to be a slow inactivation of dendritic Na^+ channels. This process may also contribute to a decrease in dendritic spike amplitude in ELL pyramidal cells observed during antidromic spike trains (Lemon and Turner 2000). As stated in the preceding text, a slow inactivation of dendritic Na^+ channels could contribute to burst discharge by reducing the activation of K^+ currents that repolarize the dendritic spike ($I_{Dr,d}$ and $I_{AptKv3.3}$ in the model).

Mickus et al. (1999) presented a detailed kinetic model of $I_{Na,d}$ inactivation that considers two separate inactivation states variables: fast and slow. Slow inactivation is the state variable that cumulatively grows from spike to spike, producing spike attenuation during repetitive discharge. To incorporate this concept into the model Hodgkin-Huxley framework, we propose to modify the existing $I_{Na,d}$ description through the addition of a second inactivation state variable $p_{Na,d}$ designed to represent a slow inactivation according to

$$I_{Na,d} = g_{max,Na,d} \cdot m_{Na,d}^2 h_{Na,d} p_{Na,d} \cdot (V_m - V_{rev,Na,d}) \qquad (4)$$

where $m_{Na,d}$ and $h_{Na,d}$ are the original fast activation and inactivation state variables introduced in METHODS. $m_{Na,d}$, $h_{Na,d}$, and $p_{Na,d}$ are each described by *Eqs. 1.2* and *1.3,* with parameters specific to the channel (see Table 1 for $m_{Na,d}$ and $h_{Na,d}$,

and the following text for $p_{Na,d}$ parameters). To our knowledge, no previous studies have characterized dendritic Na^+ slow inactivation kinetics sufficiently so as to fully justify our choice of the model parameters. We thus set the $V_{1/2,pNa,d}$ to -65 mV and $k_{pNa,d}$ to 5 mV thereby ensuring that spike backpropagation is required to significantly inactivate Na, d, similar to previous experimental observations (Colbert et al. 1997; Jung et al. 1997). However, to properly set $\tau_{p,Na,d}$, which determines both the time scale of onset and recovery from inactivation, further assumptions must be made.

Colbert et al. (1997) and Jung et al. (1997) both reported that full recovery of Na^+ channel inactivation occurred in the order of seconds. This time scale is to long reproduce ELL pyramidal cell spike bursts because significant $I_{Na,d}$ recovery needs to occur within the inter-burst interval, which is 10–15 ms (Lemon and Turner 2000). However, simply setting $\tau_{p,Na,d}$ so that recovery from Na^+ channel inactivation occurs on a 15-ms time scale also results in significant recovery from inactivation during repetitive spike discharge, removing the decrease in spike amplitude during the burst. Recovery from slow inactivation of dendritic Na^+ channels after a stimulus train has been shown to be accelerated through membrane hyperpolarization (Mickus et al. 1999). This is ideal for allowing only significant inactivation recovery of dendritic Na^+ in the inter-burst interval, which occurs in proximal apical dendrites at potentials up to -10 mV lower than intra-burst subthreshold potentials (Lemon and Turner 2000). We therefore extend the description of $\tau_{p,Na,d}$ to include voltage dependence as originally modeled by Hodgkin and Huxley (1952). Rather than using the α and β rate formalism, we simply assumed a sigmoidal relation between $\tau_{p,Na,d}$ and V_m

$$\tau_{p,Na,d}(V_m) = \frac{\tau_{max}}{(1 + e^{-(V_m - V_{1/2,\tau})/k_\tau})} \qquad (5)$$

where τ_{max} is the maximum time constant of $p_{Na,d}$, while $V_{1/2,\tau}$ and k_τ describe the voltage dependence in analogous fashion to the steady-state conductance relations given by *Eq. 1.3*. We set $V_{1/2,\tau}$ to -60 mV, k_τ to -3 mV, and τ_{max} to 20 ms to separate the $p_{Na,d}$ inactivation into two distinct time scales; slow at membrane potentials typical for intra-burst depolarizations and fast for the hyperpolarized potentials associated with the burst AHPs.

Figure 10A shows the response of the model dendritic compartment (200 μm) to two 50-ms step somatic depolarizations of 1 nA, separated by 15 ms to simulate the occurrence of a burst AHP. Spike amplitude during both trains of backpropagating model spikes show attenuation similar in both magnitude and time scale to that observed in recordings of bursting ELL pyramidal cell proximal apical dendrites (Lemon and Turner 2000). The model dendritic spikes do indeed show a full recovery from slow inactivation during a 15-ms pause between depolarizations (Fig. 10A). This indicates that the inclusion of voltage dependence of $\tau_{p,Na,d}$ produces a recovery from Na^+ channel inactivation that would be necessary to sustain bursting. Nevertheless Fig. 10B shows that under constant somatic depolarization, only rapid dendritic spike attenuation, which saturates at a fixed amplitude, and not burst discharge is observed. This pattern is identical to the attenuation and saturation of dendritic spike amplitude observed in rat CA1 pyramidal cells during antidromic repetitive stimulation (Colbert et al. 1997; Jung et al. 1997). It is also important to
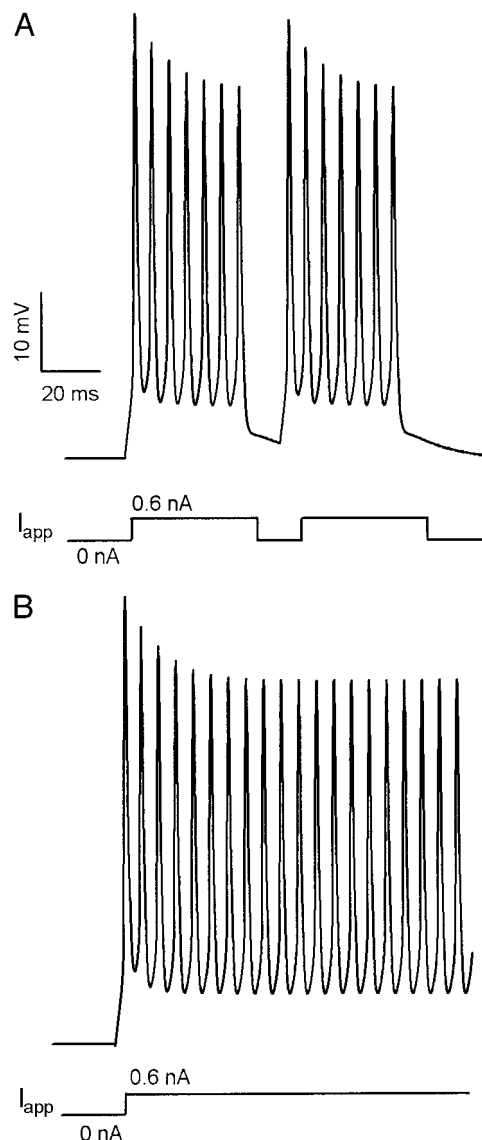
FIG. 10. Slow inactivation of $I_{Na,d}$ is not sufficient to generate conditional backpropagation and burst discharge. *A*: model dendritic voltage response (200 μm from soma) during repetitive spike discharge at ~130 Hz with slow inactivation inserted into $I_{Na,d}$ kinetics. Two depolarizing pulses (I_{app}) of 40-ms duration are applied, separated by a return to rest for 15 ms to simulate the time frame of a typical burst and burst AHP in ELL pyramidal cells in vitro. The amplitude of the dendritic spike decreases during repetitive discharge with a similar magnitude and time scale as found in ELL pyramidal cell dendrites (cf. Fig. 12*C*). The 15-ms pause in I_{app} is sufficient to allow significant recovery from $I_{Na,d}$ slow inactivation, as indicated by the identical dendritic response to both pulses. This behavior required $\tau_{p,Na,d}$ to be voltage dependent, as described by *Eq. 5*. *B*: the response of the model to a sustained I_{app} of the same magnitude as in *A* but without the 15-ms pause between pulses. Note that the steady-state discharge pattern is tonic, indicating that slow inactivation of $I_{Na,d}$ is not sufficient to cause the intermittent failure of backpropagation that characterizes burst discharge in ELL pyramidal cells.

note that significant broadening of model dendritic spikes does not occur under these conditions, and an ISI of 8 ms is sustained during repetitive discharge (Fig. 10*B*). Further adjustment of model $I_{Na,d}$ parameters does not qualitatively change these results. These simulations indicate that a cumulative inactivation of Na, d and the associated decrease in spike amplitude is not sufficient to produce burst discharge in the core model. Although this mechanism may contribute to the

processes underlying dendritic spike failure in the intact cell, we remove slow inactivation of Na, d from subsequent simulations to simplify the analysis.

Slow activation of I_{NaP}

Recent experimental studies have suggested that I_{NaP} contributes substantially to the depolarization that drives burst discharge in several mammalian neurons (Azouz et al. 1996; Brumburg et al. 2000; Franceschetti et al. 1995; Magee and Carruth 1999). In ELL pyramidal cells, we find that I_{NaP} kinetics that lead to appropriate shifts in RMP and EPSP amplitude are not able to promote burst discharge. To identify the potential for I_{NaP} to contribute to burst discharge in *Apteronotus* pyramidal cells, a slow activating component to the typical fast activating I_{NaP} is hypothesized. If such a component was added to the model description, then NaP could cumulatively grow during a burst, thereby broadening dendritic spikes. This would produce a slow growth in DAP amplitude, a reduction in spike latency to discharge, and a shortening in ISI through a burst. We modify the existing description of I_{NaP} in both somatic and dendritic compartments by creating a second activation variable, q_{NaP}, in the NaP current equation

$$I_{NaP} = g_{max,NaP} \cdot m_{NaP}^3 q_{NaP} \cdot (V - V_{rev,Na}) \qquad (6)$$

where m_{NaP} is the original activation variable, and q_{NaP} is also described by *Eqs. 1.2* and *1.3*. We force the m_{NaP} and q_{NaP} voltage dependencies to be equal by setting $V_{1/2,q,NaP}$ and $k_{q,NaP}$ to be identical to those of m_{NaP} (see Table 1). We set $\tau_{q,NaP}$ to 10 ms, which is of the same order of magnitude as burst oscillation periods observed in the ELL (Lemon and Turner); recall that $\tau_{m,NaP}$ is an order of magnitude smaller, being set to 0.3 ms. With the addition of a second state variable, the overall conductance will decrease; hence $g_{max,NaP}$ is increased by a factor of 5 in both the soma and dendrites to compensate. Figure 11*A* shows the time course of the model somatic I_{NaP} during a repetitive spike train with Fig. 11*B* showing the associated somatic voltage. A cumulative increase in I_{NaP} during repetitive spike discharge (Fig. 11*A*) produces a slow depolarizing envelope at the soma that reduces the ISI and leads to a transition from tonic to spike doublet discharge (Fig. 11*B*). The doublet firing is due to NaP promoting high-frequency spike discharge, which results in the failure of backpropagation of the second spike of the doublet, as described in Fig. 5 and Lemon and Turner (2000). The ability for I_{NaP} to promote a switch to burst discharge that incorporates conditional backpropagation is encouraging. However, we find that this mechanism is unable to generate bursts composed of four or more spikes, as is typically the case in pyramidal cells in vitro. In fact, all reasonable modifications of q_{NaP} parameters are unable to generate bursts longer than recurring spike doublets. To increase the possibility of producing realistic burst discharge, $\tau_{q,NaP}$ was made voltage dependent (not shown), with similar dependency as that described by *Eq. 5*. This causes fast deactivation of q_{NaP} during the hyperpolarization associated with inter-burst periods, and slow activation of q_{NaP} during the intra-burst depolarization. Once again, the simulations only generated doublet firing, as shown for the voltage-independent τ_{NaP} case.

As reported previously, these results indicate that I_{NaP} is capable of contributing to burst discharge in the γ-frequency
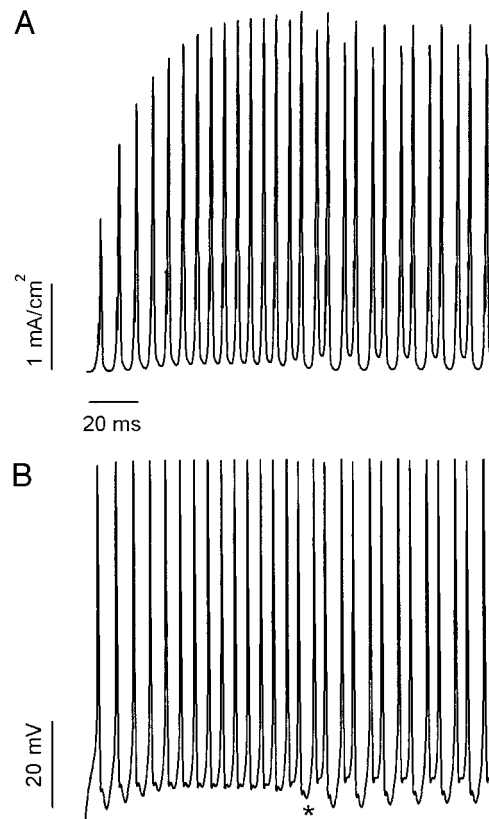

FIG. 11. Slow accumulation of I_{NaP} is insufficient to produce model burst discharge comparable to in vitro experiment. *A*: g_{NaP} response to constant depolarization (0.6 nA) that evokes repetitive spike discharge at a frequency of ~150 Hz. The conductance rapidly tracks somatic spiking through fast activation and deactivation, controlled by m_{NaP}. The slow activation, mediated by q_{NaP}, is the depolarizing envelope allowing cumulative growth of g_{NaP} from spike to spike during repetitive discharge. *B*: somatic voltage response during the same simulation described in *A*. Spike discharge frequency increases until the appearance of a spike doublet (onset of spike doublets marked by *).

range (Wang 1999). However, in ELL pyramidal cells, this current is unable to promote burst discharge without the addition of a slow activation rate into I_{NaP} channel kinetics. The failure to produce multiple spike bursts even with the slow activation time constant may be a result of the steeply nonlinear positive feedback incorporated into NaP (Fig. 6). Therefore we remove the slow activation of NaP introduced in this section from all subsequent analyses.

Cumulative inactivation of dendritic K^+ channels

Previous studies have shown that a cumulative inactivation of K^+ channels is essential for producing a frequency-dependent spike broadening (Aldrich et al. 1979; Ma and Koester 1995; Shao et al. 1999). Direct experimental evidence for the existence of a cumulatively inactivating K^+ channel within ELL pyramidal cell dendrites has yet to be established. Nonetheless the assumption is indirectly supported by the dendritic spike broadening observed during bursting (Lemon and Turner 2000) (Fig. 13). Instead of inserting a separate K^+ channel into the model, we choose to modify the dendritic K^+ channel, Dr, d, so that it inactivates substantially over the length of a burst yet remains constant during an individual action potential.

The core model Dr, d kinetics include only fast activation,

represented by the state variable $m_{Dr,d}$. To incorporate cumulative inactivation within the model, we introduce a second state variable $h_{Dr,d}$, representing inactivation, inserted into the current equation for Dr, d

$$I_{Dr,d} = g_{max,Dr,d} \cdot m_{Dr,d} h_{Dr,d} \cdot (V_m - V_{rev,Dr,d}) \qquad (7)$$

where $h_{Dr,d}$ is described by *Eqs. 1.1–1.3,* with parameters $\tau_{h,Dr,d}$, $V_{1/2,h,Dr,d}$, and $k_{h,Dr,d}$. We set the inactivation to be low threshold ($V_{1/2,h,Dr,d} = -65$ mV), steeply nonlinear ($k_{h,Dr,d} = -6$), and following a time course so that its inactivation is substantial over the length of a burst, yet negligible during an individual spike ($\tau_{h,Dr,d} = 5$ ms). Modification of these parameters will be explored later.

Figure 12 (*A* and *B*) illustrates the effects of incorporating cumulative inactivation of Dr, d into the core model according to *Eq. 7.* The qualitative change from nonbursting to bursting behavior is evident. Direct comparisons to experimental data are presented in the following text. Figure 12*C* plots the state variable $h_{Dr,d}$ from the same simulation as in Fig. 12*B*. The slow increase of inactivation ($h_{Dr,d}$ decreases) occurs over the length of each individual burst. At burst termination, inactivation is removed quickly ($h_{Dr,d}$ increases) due to the large hyperpolarization associated with a burst AHP (bAHP), and slow inactivation begins again with the next burst. Because of the addition of this second state variable, $h_{Dr,d}$, which oscillates between values of 0.3 and 0.1 during bursting, $g_{max,Dr,d}$ is increased from 0.2 to 0.65 S/cm² to compensate. This ensures that the current $I_{Dr,d}$ remains comparable between nonbursting and bursting models.

Figure 13 compares in detail the characteristics of burst discharge in ELL pyramidal cells to burst simulations when a cumulative inactivation of $I_{Dr,d}$ is incorporated into the model. Shown are somatic and dendritic recordings of a single spike burst with the equivalent simulation results at the same scale below. Comparing the somatic recording and simulation (Fig. 13, *A* and *B*) reveals that the model successfully reproduces a progressive increase in the DAP, a reduction in ISI during the burst, and a high-frequency spike doublet that is followed by a large-amplitude burst AHP; all characteristic and key elements in the process of conditional spike backpropagation (Lemon and Turner 2000). Note that potentiation of the DAP in the model occurs at the same initial intra-burst ISI as pyramidal cells, with a matching decrease in ISI over the course of a six-spike burst. The final burst frequency in both experiment and simulation is 25 Hz (not shown), within the expected range of oscillatory burst frequency near burst threshold (Lemon and Turner 2000). At the dendritic level (Fig. 13, *C* and *D*), the model now reproduces a progressive frequency-dependent spike broadening that underlies a temporal summation of dendritic spikes (Fig. 13, *C* and *D, insets*). This temporal summation leads to the further development of a depolarizing envelope that contributes to potentiation of the DAP at the soma. The dendritic simulation also correctly replicates the conditional failure of spike backpropagation when a spike doublet is generated at the soma as indicated by a passively reflected partial spike response at the end of the simulated burst (Fig. 13*D*). Finally, the hyperpolarization produced by the bAHP is sufficient to promote recovery from $I_{Dr,d}$ inactivation (Fig. 12*C*), essentially resetting the duration of dendritic spikes to allow the cell to repeat this process and generate the next burst.

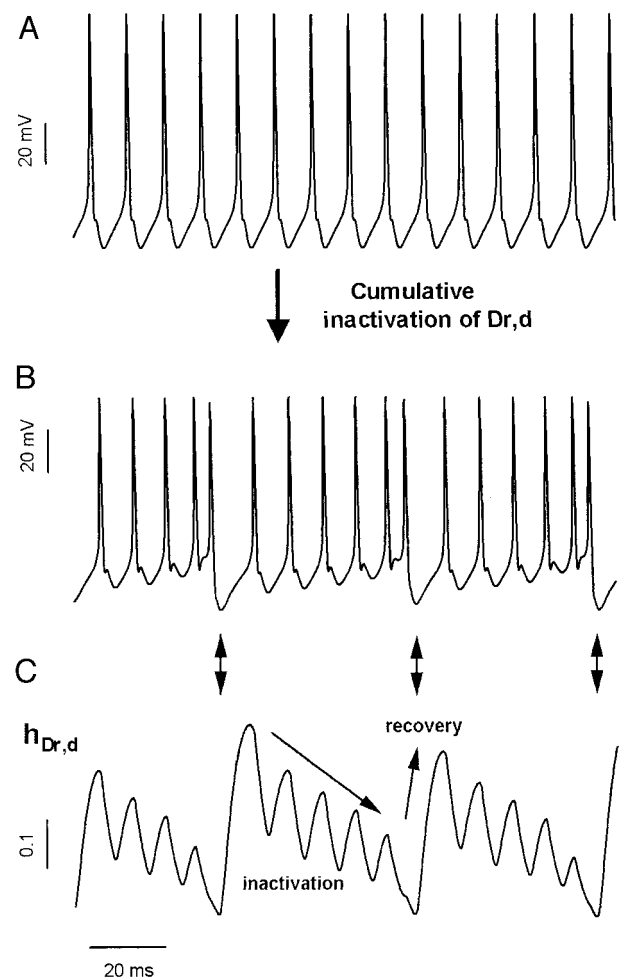One discrepancy between the dendritic simulation and ex-

FIG. 12. Cumulative inactivation of the dendritic K⁺ current $I_{Dr,d}$ is sufficient to promote burst discharge. All simulations have a depolarizing current of 0.6 nA applied to the somatic compartment. *A*: the core model generates only repetitive somatic spike discharge in response to depolarization. *B*: cumulative inactivation of $I_{Dr,d}$ promotes a gradual decrease in the ISI, an increase in DAP amplitude, and spike doublet discharge and subsequent bAHP associated with conditional spike backpropagation. *C*: the dynamics of the gating variable $h_{Dr,d}$ as the burst shown in *B* evolves. The cumulative inactivation occurs as $h_{Dr,d}$ decreases slowly during a burst. Removal of inactivation occurs rapidly with the bAHP that follows each spike doublet (↕).

perimental recordings is the lack of dendritic spike attenuation in the model output (Fig. 13*D*). Although the ionic mechanism underlying this process in pyramidal cells is unknown, it may involve a slow inactivation of dendritic Na⁺ channels as modeled in Fig. 10. However, the results of Fig. 13 clearly indicate that it is not essential to reproducing the major features of burst discharge. Hence, for simplicity, it is not incorporated into the model at this time.

It should be noted that the voltage and time dependencies of $I_{Dr,d}$ inactivation, $h_{Dr,d}$, are chosen so as to best reproduce the experimental data. In fact, several characteristics of burst output depend strongly on the kinetic properties of $I_{Dr,d}$ inactivation. Specifically, reduction of $\tau_{Dr,d}$ 2 ms removes all burst output from the simulations, indicating that $I_{Dr,d}$ inactivation must be cumulative to achieve burst discharge. Setting $\tau_{Dr,d}$ to values above 2 ms does not prevent bursting but rather modifies burst frequency, with $\tau_{Dr,d} > 10$ ms producing oscillatory burst discharge outside the γ-frequency range (<20 Hz). Re-
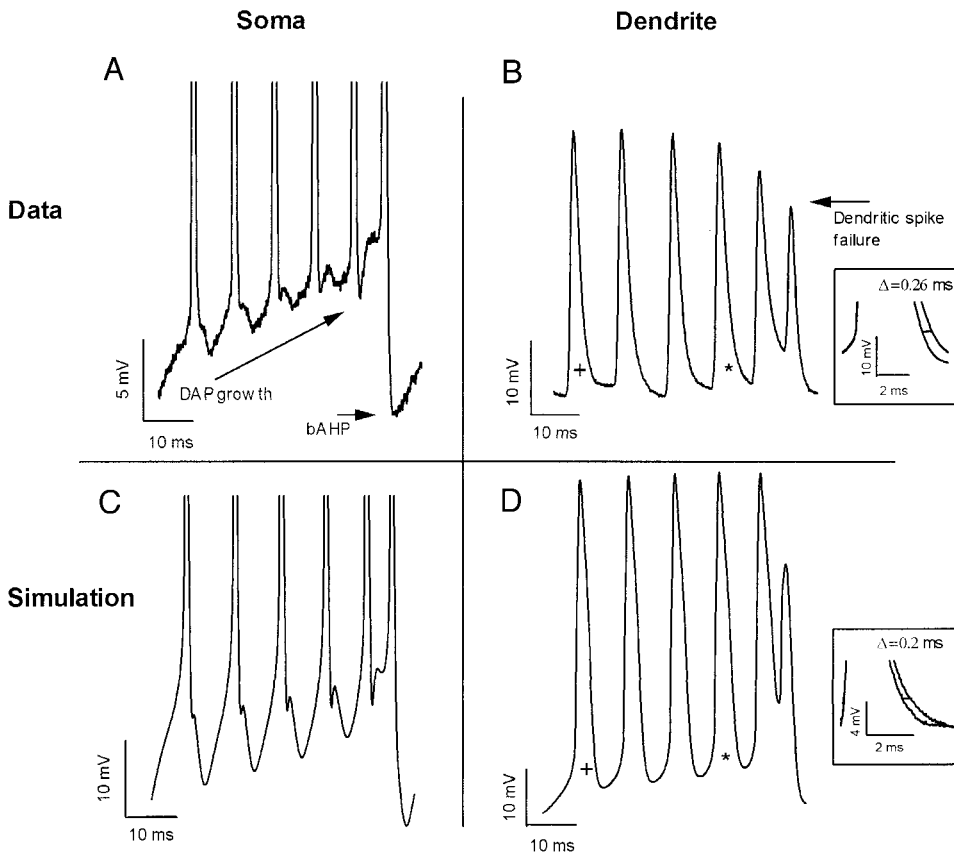
FIG. 13. A comparison between simulated burst discharge and experimentally recorded bursts in ELL pyramidal cells. *A* and *B*: somatic and dendritic burst trains recorded from ELL pyramidal cells [see Lemon and Turner (2000) for experimental protocol]. In pyramidal cell somatic recordings (*A*), a potentiation of the DAP and a burst AHP (bAHP) at the end of a burst are prominent (arrows). Dendritic recordings (*B*) are associated with a frequency-dependent broadening of the dendritic spike and final failure (arrow) on generation of a spike doublet at the soma. *Inset*: a magnified and superimposed view of the base of spikes marked by the plus and the asterisk in the dendritic recording to reveal a difference of 0.26 ms (Δ) in dendritic spike durations. *C* and *D*: model somatic and dendritic burst response with $I_{app} = 0.6$ nA. The model somatic train (*C*) indicates the same pattern of DAP potentiation at the soma, dendritic spike summation and broadening, spike doublet and bAHP as found in ELL pyramidal cell recordings (*A*). The model duration of the indicated dendritic spikes (as in *B*) are again shown in expanded form in the *inset*.

alistic modifications of $k_{h,Dr,d}$ do not qualitatively change burst output in the model. However, increases or decreases of $V_{1/2,h,Dr,d}$ outside the voltage range attained by dendritic spikes (below -80 or above -20 mV) blocks burst discharge. This again emphasizes the importance of the properties of backpropagating dendritic spikes in activating and inactivating $I_{Dr,d}$ channels to bring about burst discharge.

Dissection of the burst mechanism

We investigated the role of several potential ionic mechanisms to simulate ELL pyramidal cell γ-frequency burst discharge. We could not match experimental results for γ-frequency burst output by introducing a slow activation of somatic K^+ conductance, a slow inactivation of Na, d channels, or a slow activation of NaP, indicating that these conditions are not by themselves sufficient components of the burst mechanism. In contrast, introducing a cumulative inactivation of dendritic K^+ current was very successful in producing a realistic burst output, suggesting that this mechanism is an essential factor in pyramidal cell γ bursting. We now dissect the complete burst mechanism into the main ionic currents that underlie its evolution and termination.

We first elicit a single burst by somatic depolarization, shown in Fig. 14*A* complete with spike doublet and bAHP; all subsequent analysis will pertain to this burst. Figure 14*B* plots the time series of the channel conductance $g_{Dr,d}$ from the apical dendritic compartment 200 μm from the soma (last active zone) over the duration of the burst. Recall that $g_{Dr,d} = g_{max,Dr,d} \cdot m_{Dr,d}h_{Dr,d}$, where $m_{Dr,d}$ and $h_{Dr,d}$ are the respective activation and cumulative inactivation parameters of the den-

dritic K^+ channel. Figure 14*B* shows the conductance of Dr, d tracking each spike in the burst as it activates and deactivates quickly (the activation time constant $\tau_{m,Dr,d} = 0.9$ ms). A cumulative inactivation is clear from the attenuation of $g_{Dr,d}$ that occurs during the burst. This attenuation leads to dendritic spike broadening and a temporal summation of dendritic spikes that produces a slow depolarizing envelope (Fig. 13). The combination of an increase in dendritic spike duration and a slow depolarizing envelope allows the DAP at the soma to increase from spike to spike during the burst. The increase in the DAP further depolarizes the soma to reduce the ISI as the burst evolves. Thus cumulative inactivation of a dendritic K^+ channels is sufficient in itself to account for each of the key properties of spike discharge that characterize burst generation in pyramidal cells (Lemon and Turner 2000). Another factor that merits further consideration in future electrophysiological studies is the kinetic properties of I_{NaP} that might contribute to the dendritic depolarization observed during repetitive discharge.

The termination of the burst is quite separate from the mechanism driving spike discharge. Figure 14*C* plots $g_{Na,d}$, the dendritic Na^+ conductance 200 μm from the soma during the length of the burst. Recall that the conductance is given by $g_{Na,d} = g_{max,Na,d}$ and $m_{Na,d}h_{Na,d}$. Here $g_{Na,d}$ decreases slightly with each spike in the burst but exhibits a pronounced decrease on the generation of a spike doublet at the end of the spike train (Fig. 14*C*). This corresponds to a failure of spike backpropagation when the high frequency of the spike doublet exceeds the dendritic refractory period as reflected by the significant drop in $g_{Na,d}$ on the final spike. In contrast, doublet frequencies of firing can easily be sustained by the somatic conductance
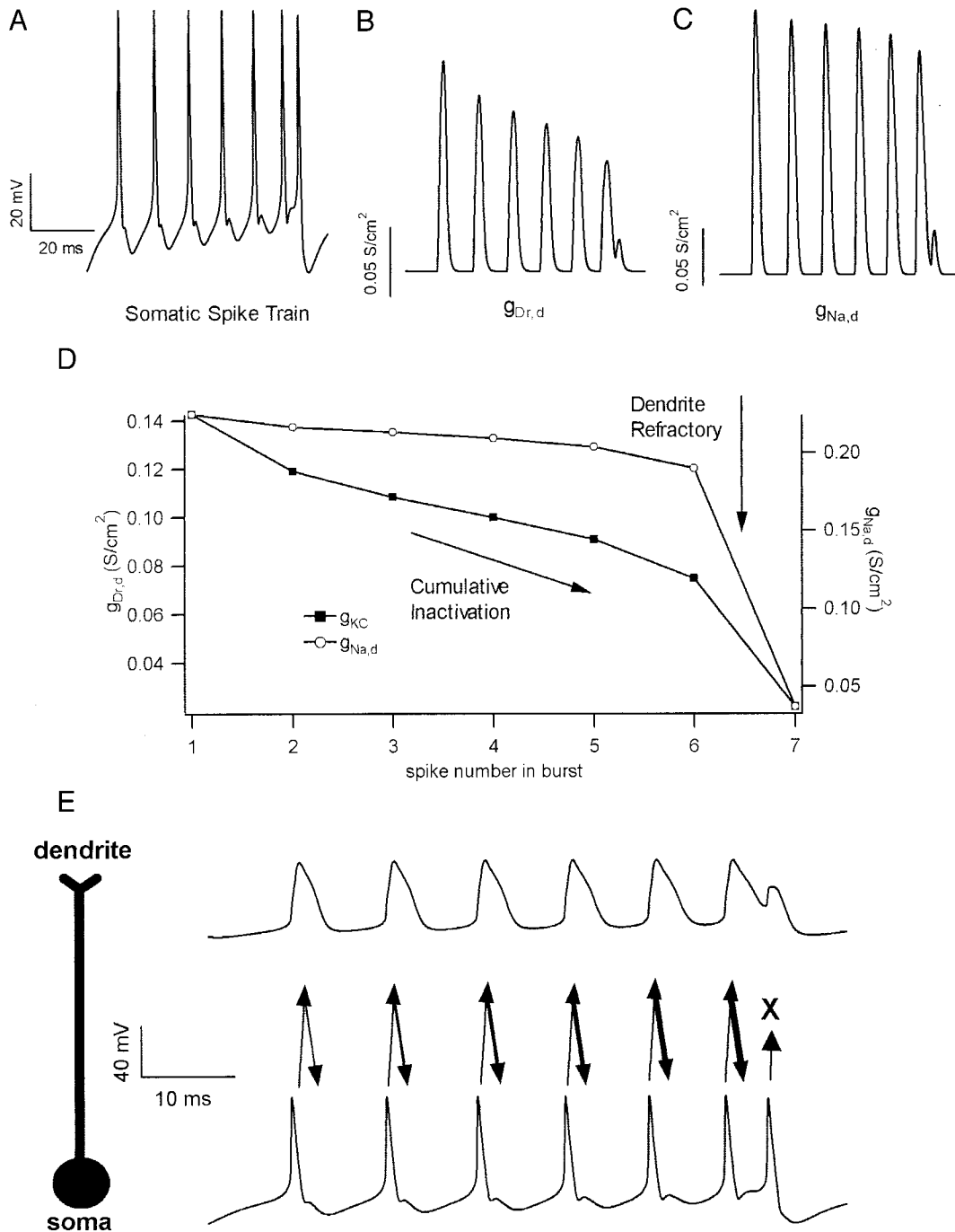
FIG. 14. Analysis of the burst mechanism in pyramidal cells. *A*: the potential at the soma during a burst simulation, including termination by a spike doublet and bAHP. This burst is used in the analysis of the other panels. The time calibration shown also applies to *B* and *C*. *B*: a plot of $g_{Dr,d}$ as the burst shown in *A* evolves indicates a cumulative inactivation that steadily reduces peak conductance during repetitive discharge. *C*: a plot of $g_{Na,d}$ as the burst shown in *A* evolves. The conductance peak shows a slight decrease until the spike doublet at the end of the burst, at which point the ISI is inside the refractory period of $I_{Na,d}$ and hence the channel cannot respond. Dendritic backpropagation then fails, preventing the current flow that produces a DAP at the soma. *D*: plots of the peak conductance of $g_{Dr,d}$ (*B*) and $g_{Na,d}$ (*C*) as a function of spike number for the burst shown in *A*. The slow drop in $g_{Dr,d}$ due to cumulative inactivation is shown as well as the complete failure of $g_{Na,d}$ at the occurrence of the spike doublet when spike frequency exceeds the dendritic refractory period. *E*: a schematic diagram of the soma-dendritic interactions that underlies conditional backpropagation in the simulation. The burst begins with initiation of a spike at the soma which backpropagates over ~200 μm of the apical dendrite through the activation of $I_{Na,d}$ (upward arrow). The long duration of the dendritic spike compared with somatic spike results in return current flow to generate a DAP at the soma (downward arrow). The DAP depolarizes the soma, thereby contributing to the next spike. Cumulative inactivation of $I_{Dr,d}$ during repetitive discharge increases dendritic spike width and thus the depolarization that determines DAP amplitude and duration (shown by an increasing width of the downward arrows). The increase in the somatic DAP reduces subsequent ISIs in the burst until triggering a final spike doublet. At spike doublet frequencies dendritic membrane is refractory and backpropagation fails, removing the DAP at the soma (small arrow blocked by an X). The sudden loss of dendritic depolarization uncovers a large somatic bAHP, which hyperpolarizes the soma and terminates the burst.

$g_{Na,s}$ (not shown), allowing two full somatic spikes to be generated (Fig. 14*A*). When the dendritic spike fails to activate, the DAP is selectively removed at the somatic level, uncovering a large bAHP that signifies the end of a spike burst (Fig. 14*A*). To test the significance of the dendritic refractory period for burst generation, we performed additional simulations where $I_{Na,d}$ was replaced by $I_{Na,s}$, thereby establishing equivalent dendritic and somatic refractory periods. Spike bursts do not occur in these simulations with only repetitive discharge observed for all levels of depolarizing somatic current injection. Hence the longer refractory period of the dendrite as compared with the soma is necessary for burst termination as proposed by Lemon and Turner (2000).

The ionic basis of the bAHP has not been fully determined, but the initial early phase of this response is insensitive to both TEA and Cd^{2+}, eliminating many candidate K^+ currents in pyramidal cells that could actively contribute to the bAHP (Noonan et al. 2000). However, we should note that the large hyperpolarization of the model bAHP is also due to slight summation of the somatic I_{KA} (τ_{KA} = 1 ms) that occurs only at doublet frequencies (data not shown). Although this effect enhances burst termination, elimination of I_{KA} does not prevent bursting in the model.

Figure 14*D* presents the cumulative inactivation of $g_{Dr,d}$ and the sudden failure of $g_{Na,d}$ as a function of spike number of the burst presented in Fig. 14*A*. This superimposes the results of Fig. 14, *B* and *C*, and considers the evolution and termination of the burst as events driven by action potentials. Figure 14*E* schematically summarizes the burst mechanism by considering the end effect of $I_{Dr,d}$ and $I_{Na,d}$ in shaping the soma-dendritic interaction. Their action results in a cumulative DAP growth and eventually a sharp DAP failure that is the manifestation of the burst mechanism presented in Fig. 14, *B–D,* at the level of membrane voltage.

The currents I_A and I_{KB} were included for all bursting simulations. However, the presence of these channels is not required for model bursting (data not shown). This is clear because I_A requires hyperpolarization to remove inactivation and therefore was inactivated at the depolarized membrane potentials required for bursting. I_{KB} has a time course in the order seconds and can be approximated as static on the short time scale of bursting.

DISCUSSION

Importance of a realistic model of ELL pyramidal cells

Recently the ELL has been the focus of numerous investigations into the role of bursting in sensory information processing (Gabbiani and Metzner 1999; Gabbiani et al. 1996; Metzner et al. 1998). Feedforward information transfer is currently under study in the ELL through modeling of P-afferent dynamics and coding (Chacron et al. 2000; Kreiman et al. 2000; Nelson et al. 1997; Ratnam and Nelson 2000; Wessel et al. 1996). Studies of synaptic feedback to the ELL involve both experimental and computational work (Berman and Maler 1998a–c; 1999; Berman et al. 1997; Doiron et al. 2001; Nelson 1994). In fact recent experimental work has suggested that feedback activity modulates bursting behavior in ELL pyramidal cells (Bastian and Nguyenkim 2001). The subtle nature of these issues points to the usefulness of a detailed and realistic

compartmental model for creating and testing hypotheses concerning burst mechanisms and their regulation by feedforward and feedback synaptic input.

ELL burst mechanism

Our results suggest the following necessary and sufficient conditions for ELL pyramidal cell bursting. First, there must be a dendritic Na^+ current to support spike backpropagation into the proximal apical dendrites, yielding a DAP at the soma. Second, there must be a (proposed) cumulative inactivation of a K^+ conductance involved in dendritic spike repolarization. This inactivation effectively results in a dendritic spike broadening during repetitive discharge that is known to potentiate DAP amplitude at the soma. Finally there must be a longer spike refractory period in the dendrites compared with the soma, causing backpropagation to be conditional on the somatic spike discharge frequency, which terminates a burst at sufficiently high discharge rates.

AptKv3.3 as a possible candidate for Dr, d

In the present study, we assigned kinetic properties to the Dr, d channel that allow it to be activated by dendritic spikes and to exhibit cumulative inactivation during repetitive spike discharge by virtue of a relatively low $V_{1/2}$ for inactivation. It is important to note that the Dr, d channel is a hypothetical channel subtype inserted in the model to allow for proper simulation of the dendritic spike response. The question remains as to which, if any, dendritic channel in intact ELL pyramidal cells matches the description of Dr, d. One potential current is *Apt*Kv3.3, which is located with high prevalence over the entire axis of pyramidal cells (Rashid et al. 2001). Indeed, pharmacological blockade of dendritic *Apt*Kv3 channels has been shown to decrease dendritic spike repolarization and lower the threshold for burst discharge (Rashid et al. 2001). The possibility therefore exists that dendritic *Apt*Kv3.3 K^+ channels may serve a similar capacity as the Dr, d channels in the current model.

We modeled $I_{AptKv3.3}$ according to the kinetic properties inherent to whole cell currents when *Apt*Kv3.3 channels are transiently expressed in HEK cells (Rashid et al. 2001). These currents share several properties with Dr, d channels, including fast activation and deactivation kinetics. The major difference is the $V_{1/2}$ of activation: $V_{1/2,m,Dr,d}$ = −40 mV and $V_{1/2,m,AptKv3.3}$ = 0 mV. We found that burst discharge can still be produced in the model if $V_{1/2,m,Dr,d}$ is raised no higher than −20 mV with corresponding adjustments to channel density to offset the smaller degree of current activation. However, with $V_{1/2,m,Dr,d}$ > −20 mV, the model could not produce bursting with realistic values of $g_{max,Dr,d}$. Similarly, *Apt*Kv3.3 as modeled in the cell could not produce bursting with a $V_{1/2}$ of 0 mV, even if a cumulative inactivation similar to Dr, d was introduced (results not shown). We have recently begun to characterize an additional slow inactivation process in *Apt*Kv3.3 channels that has not been incorporated into the present model. Recent work further indicates that the $V_{1/2}$ for *Apt*Kv3.3 slow inactivation can exhibit a leftward (negative) shift in the outside-out as compared with whole cell recording configuration (Morales and Turner, unpublished observations). This suggests that *Apt*Kv3.3 kinetics are subject to second-messenger regu-

lation as previously shown for other Kv3 channel subtypes (Atzori et al. 2000; Covarrubias et al. 1994; Moreno et al. 1995; Velasco et al. 1998). The potential therefore exists for a selective modulation of dendritic *Apt*Kv3.3 kinetics that would allow this channel to exhibit a cumulative inactivation during repetitive spike discharge. Further experimental work will be needed to determine the exact voltage-dependence and regulation of somatic versus dendritic *Apt*Kv3.3 channels to test this hypothesis.

Relation to in vivo bursting

A recent quantitative analysis of burst discharge in ELL pyramidal cells has shown that the ISIs during spontaneous bursts recorded in vivo remain relatively constant, and often lack a terminating spike doublet; results that differ from the burst mechanism routinely recorded in vitro (Bastian and Nguyenkim 2001). At present the discrepancy between the bursts that are driven by current-evoked depolarizations in vitro and baseline discharge recorded in vivo is not clear. There are many differences between the state of pyramidal cells in vivo versus in vitro: the resting membrane potential of pyramidal cells in vivo is closer to spike threshold (J. Bastian, personal communication), the input resistance of pyramidal cells is likely to be far lower in vivo because of synaptic bombardment (Bernander et al. 1991; Paré et al. 1998; Bastian, personal communication), stimulation in vitro is via constant current injection, whereas in vivo the primary stimulus is a stochastic synaptic input to dendrites, and in vivo studies contain network effects which in vitro studies necessarily lack. Further exploration with the model ionic channel parameters, to modify these features, as well introducing simulated synaptic input, may bridge the gap between in vivo and in vitro results. However, more detailed experimental analysis is required before any modeling attempt is to be made along these lines.

Application of ELL burst model to mammalian chattering cells

Sustained γ-frequency bursting, or chattering behavior, has been observed in mammalian cortical neurons (Brumburg et al. 2000; Gray and McCormick 1996; Llinás et al. 1991) and corticothalamic neurons (Steriade et al. 1998). Wang (1999) produced a "chattering" behavior in a two-compartment neuron model that incorporates a similar "ping-pong" reciprocal interaction between the cell soma and dendrites we have described in ELL pyramidal cells. The evolution and termination of the burst in Wang's model relies on a cumulative activation of $K_{(Ca)}$. This produces a characteristic increase of intra-burst ISIs and a prominent DAP in the inter-burst interval (Wang 1999). We have shown (Fig. 9) that this mechanism is not able to produce realistic ELL pyramidal cell bursts because it fails to reproduce a decrease in intra-burst ISIs, the slow somatic depolarization that increases the DAP, and the lack of a DAP at burst termination as observed with pyramidal cells in vitro (Lemon and Turner 2000). Our proposed mechanism successfully reproduces all the preceding criteria. Brumburg et al. (2000) report the cumulative reduction of spike fAHPs as a burst evolves in supragranular cortical neurons. This result also cannot be reproduced by cumulative activation of $K_{(Ca)}$ in our

model, as used in Wang (1999) or in other detailed IB neuron compartmental models (Mainen and Sejnowski 1996; Pinsky and Rinzel 1994; Rhodes and Gray 1994; Traub et al. 1994). Brumberg et al. (2000) hypothesize that the mechanism underlying γ-burst discharge in mammalian visual cortex could be either a slow increase of a Na^+ current or a slow decrease of a K^+ current. Our modeling of ELL pyramidal cells reveals that cumulative inactivation of a dendritic K^+ current can play a key role in generating burst discharge, a result that may have wide applicability to cells discharging in the γ-frequency range.

The NEURON codes for our ELL pyramidal cell model are freely available at http://www.science.uottawa.ca/phy/grad/doiron/

REFERENCES

ALDRICH R, GETTING P, AND THOMSON S. Mechanism of frequency-dependent broadening of molluscan neuron soma spikes. *J Physiol (Lond)* 291: 531–544, 1979.

ANDREASEN M AND LAMBERT JDC. Somatic amplification of distally generated subthreshold EPSPs in rat hippocampal pyramidal neurons. *J Physiol (Lond)* 519: 85–100, 1999.

ATZORI M, LAU D, TANSEY EP, CHOW A, OZAITA A, RUDY B, AND MCBAIN CJ. H2 histamine receptor-phosphorylation of Kv3.2 modulates interneuron fast spiking. *Nat Neurosci* 3: 791–798, 2000.

AZOUZ R, JENSEN M, AND YAARI Y. Ionic basis of spike after-depolarization and burst generation in adult rat hippocampal CA1 pyramidal cells. *J Physiol (Lond)* 492: 2111–223, 1996.

BASTIAN J. Electrolocation. I. How the electroreceptors of *Apteronotus albifrons* code for moving objects and other electrical stimuli. *J Comp Physiol [A]* 144: 465–479, 1981.

BASTIAN J AND NGUYENKIM J. Dendritic modulation of burst-like firing in sensory neurons. *J Neurophysiol* 85: 10–22, 2001.

BERMAN N, DUNN RJ, AND MALER L. Function of NMDA receptors and persistent sodium channels in a feedback pathway of the electrosensory system. *J Neurophysiol* 86: 1612–1621, 2001.

BERMAN NJ AND MALER L. Inhibition evoked from primary afferents in the electrosensory lateral line lobe of the weakly electric fish. *J Neurophysiol* 80: 3173–3196, 1998a.

BERMAN NJ AND MALER L. Interaction of GABA_B-mediated direct feedback inhibition with voltage-gated currents of pyramidal cells in the electrosensory lateral line lobe. *J Neurophysiol* 80: 3197–3213, 1998b.

BERMAN NJ AND MALER L. Distal vs proximal inhibitiory shaping of feedback excitation in the lateral line lobe. *J Neurophysiol* 80: 3214–3232, 1998c.

BERMAN NJ AND MALER L. Neural architecture of the electrosensory lateral line lobe: adaptations for coincidence detection, a sensory searchlight and frequency-dependent adaptive filtering. *J Exp Biol* 202: 1243–1253, 1999.

BERMAN NJ, PLANT J, TURNER RW, AND MALER L. Excitatory amino acid receptors at a feedback pathway in the electrosensory system: implications for the searchlight hypothesis. *J Neurophysiol* 78: 1869–1881, 1997.

BERNANDER O, DOUGLAS RJ, MARTIN KA, AND KOCH C. Synaptic background activity influences spatiotemporal integration in single pyramidal cells. *Proc Natl Acad Sci USA* 88: 11569–11573, 1991.

BRUMBERG JC, NOWAK LG, AND MCCORMICK DA. Ionic mechanisms underlying repetitive high-frequency burst firing in supragranular cortical neurons. *J Neurosci* 20: 4829–4843, 2000.

BUZSÁKI G AND CHROBAK J. Temporal structure in spatially organized neuronal ensembles: a role for interneuronal networks. *Curr Opin Neurobiol* 5: 504–510, 1995.

CALLAWAY JC AND ROSS WN. Frequency-dependent propagation of sodium action potentials in dendrites of hippocampal CA1 pyramidal neurons. *J Neurophysiol* 74: 1395–1403, 1995.

CHACRON MJ, LONGTIN A, ST-HILAIRE M, AND MALER L. Suprathreshold stochastic firing dynamics with memory in P-type electroreceptors. *Phys Rev Lett* 85: 1576–1579, 2000.

CHAY TR AND KEIZER J. Minimal model for membrane oscillations in the pancreatic β-cell. *Biophys J* 42: 181–190, 1983.

COLBERT C, MAGEE JC, HOFFMAN DA, AND JOHNSTON D. Slow recovery from inactivation of Na^+ channels underlies the activity-dependent attenuation of dendritic action potentials in hippocampal CA1 pyramidal neurons. *J Neurosci* 17: 6512–6521, 1997.

CONNOR JA AND STEVENS CF. Voltage clamp studies of a transient outward current in gastropod neural somata. *J Physiol (Lond)* 213: 21–30, 1971.

CONNORS BW AND GUTNICK MJ. Intrinsic firing patterns of diverse neocortical neurons. *Trends Neurosci* 13: 99–104, 1990.

CONNORS BW, GUTNICK MJ, AND PRINCE DA. Electrophysiological properties of neocortical neurons in vitro. *J Neurophysiol* 48: 1302–1320, 1982.

COVARRUBIAS M, WEI A, SALKOFF L, AND VYAS TB. Elimination of rapid potassium channel inactivation by phosphorylation of the inactivation gate. *Neuron* 13: 1403–1412, 1994.

CRITZ SD, WIBLE BA, LOPEZ HS, AND BROWN AM. Stable expression and regulation of a rat brain K^+ channel. *J Neurochem* 60: 1175–1178, 1993.

DE SCHUTTER E AND BOWER JM. An active membrane model of the cerebellar purkinje cell. I. Simulation of current clamps in slice. *J Neurophysiol* 71: 375–400, 1994.

DOIRON B, LONGTIN A, BERMAN NJ, AND MALER L. Subtractive and divisive inhibition: effect of voltage-dependent inhibitory conductances and noise. *Neural Comp* 13: 227–248, 2001.

DOIRON B, TURNER RW, LONGTIN A, MORALES E, AND MALER L. Novel bursting model of electrosensory lateral line lobe pyramidal cells (Abstract). *XXX Proc Soc Neurosci* 26: 896, 2000.

FANCESCHETTI S, GUATEO E, PANZICA F, SANCINI G, WANKE E, AND AVANZINI A. Ionic mechanism underlying burst firing in pyramidal neurons: intracellular study in rat sensorimotor cortex. *Brain Res* 696: 127–139, 1995.

FRENCH CR, SAH P, BUCKETT KT, AND GAGE PW. A voltage-dependent persistent sodium current in mammalian hippocampal neurons. *J Gen Physiol* 95: 1139–1157, 1990.

GABBIANI F AND METZNER W. Encoding and processing of sensory information in neuronal spikes trains. *J Exp Biol* 202: 1267–1279, 1999.

GABBIANI F, METZNER W, WESSEL R, AND KOCH C. From stimulus encoding to feature extraction in weakly electric fish. *Nature* 384: 564–567, 1996.

GOLDING NL AND SPRUSTON N. Dendritic sodium spikes are variable triggers of axonal action potentials in hippocampal CA1 pyramidal neurons. *Neuron* 21: 1189–1200, 1998.

GRAY CM AND MCCORMICK DA. Chattering cells: superficial pyramidal neurons contributing to the generation of synchronous oscillations in the visual cortex. *Science* 274: 109–113, 1996.

GRAY C AND SINGER W. Stimulus-specific neuronal oscillations in orientation columns of cat visual cortex. *Proc Natl Acad Sci USA* 86: 1698–1702, 1989.

HÄUSSER M, SPRUSTON N, AND STUART G. Diversity and dynamics of dendritic signaling. *Science* 290: 739–744, 2000.

HINES M AND CARNEVALE N. The neuron simulation environment. *Neural Comp* 9: 1179–1209, 1997.

HODGKIN A AND HUXLEY A. A quantitative description of membrane current and its application to conduction and excitation in nerve. *J Physiol (Lond)* 117: 500–544, 1952.

HOFFMAN DA, MAGEE JC, COLBERT CM, AND JOHNSTON D. K^+ channel regulation of signal propagation in dendrites of hippocampal pyramidal neurons. *Nature* 387: 869–875, 1997.

HUGUENARD JR. Low-threshold calcium currents in central nervous system neurons. *Annu Rev Physiol* 58: 299–327, 1996.

HUGUENARD JR AND MCCORMICK DA. Simulation of the currents involved in rhythmic oscillations in thalamic relay neurons. *J Neurophysiol* 68: 1373–1383, 1992.

IZHIKEVICH EM. Neural excitability spiking and bursting. *Int J Bifur Chaos* 10: 1171–1269, 2000.

JENSEN M, AZOUZ R, AND YAARI Y. Variant firing patterns in rat hippocampal pyramidal cells modulated by extracellular potassium. *J Neurophysiol* 71: 831–839, 1994.

JENSEN M, AZOUZ R, AND YAARI Y. Spike after-depolarization and burst generation in adult rat hippocampal CA1 pyramdial cells. *J Physiol (Lond)* 492: 199–210, 1996.

JOHNSON D AND MIAO-SIN WU S. *Foundations of Cellular Neurophysiology.* Cambridge, MA: MIT Press, 1997.

JUNG H-Y, MICKUS T, AND SPRUSTON N. Prolonged sodium channel inactivation contributes to dendritic action potential attenuation in hippocampal pyramidal neurons. *J Neurosci* 17: 663–6646, 1997.

KOCH C, BERNANDER O, AND DOUGLAS R. Do neurons have a voltage or a current threshold for action potential initiation? *J Comp Neurosci* 2: 63–82, 1995.

KREIMAN G, KRAHE R, METZNER W, KOCH C, AND GABBIANI F. Robustness and variability of neuronal coding by amplitude-sensitive afferents in the weakly electric fish *Eigenmannia*. *J Neurophysiol* 84: 189–204, 2000.

LEMON N AND TURNER RW. Conditional spike backpropagation generates burst discharge in a sensory neuron. *J Neurophysiol* 84: 1519–1530, 2000.

LIPOWSKY R, GILLESSEN T, AND ALZHEIMER C. Dendritic Na^+ channels amplify EPSPs in hippocampal CA1 pyramidal cells. *J Neurophysiol* 76: 2181–2191, 1996.

LISMAN JE. Bursts as a unit of neural information: making unreliable synapses reliable. *Trends Neurosci* 20: 28–43, 1997.

LLINÁS RR, GRACE AA, AND YAROM Y. *In vitro* neurons in mammalian cortical layer 4 exhibit intrinsic oscillatory activity in the 10- to 50-Hz frequency range. *Proc Natl Acad Sci USA* 88: 897–901, 1991.

LO F-S, CORK J, AND MIZE RR. Physiological properties of neurons in the optic layer of the rat's superior colliculus. *J Neurophysiol* 80: 331–343, 1998.

MA M AND KOESTER J. Consequences and mechanisms of spike broadening of R20 cells in *Aplysia Californica*. *J Neurosci* 15: 6720–6734, 1995.

MAGEE JC AND CARRUTH M. Dendritic voltage-gated ion channel regulate the action potential firing mode of hippocampal CA1 pyramidal neurons. *J Neurophysiol* 82: 1895–1901, 1999.

MAGEE JC AND JOHNSTON D. Characterization of single voltage-gated Na^+ and Ca^{2+} channels in apical dendrites of rat CA1 pyramidal neurons. *J Physiol (Lond)* 487: 67–90, 1995.

MAINEN ZF, JOERGES J, HUGUENARD JR, AND SEJNOWSKI TJ. A model of spike initiation in neocortical pyramidal cells. *Neuron* 15: 1427–1439, 1995.

MAINEN ZF AND SEJNOWSKI TJ. Influence of dendritic structure on firing pattern in model neocortical neurons. *Nature* 382: 363–365, 1996.

MAINEN ZF AND SEJNOWSKI TJ. Modeling active dendritic processes in pyramidal neurons. In: *Methods in Neuronal Modeling* (2nd ed.), edited by Segev I and Koch C. Cambridge MA: MIT Press, 1998, p. 313–360.

MALER L. The posterior lateral line lobe of certain gymnotoid fish: quantitative light microscopy. *J Comp Neurol* 183: 323–363, 1979.

MASON A AND LARKMAN A. Correlations between morphology and electrophysiology of pyramidal neurons in slices of rat visual cortex. II. Electrophysiology. *J Neurosci* 10: 1415–1428, 1990.

MATHIESON WB AND MALER L. Morphological and electrophysiological properties of a novel in vitro preparation: the electrosensory lateral line lobe slice. *J Comp Physiol* 163: 489–506, 1988.

MCCORMICK DA. Functional properties of a slowly inactivating potassium current in guinea pig dorsal lateral geniculate relay neurons. *J Neurophysiol* 66: 1176–1189, 1991.

MCCORMICK DA, CONNORS BW, LIGHTHALL JW, AND PRINCE DA. Comparative electrophysiology of pyramidal and sparsely spiny stellate neurons of the neocortex. *J Neurophysiol* 54: 782–806, 1985.

MCCORMICK DA AND HUGUENARD J. A model of electrophysiological properties of thalamocortical relay neurons. *J Neurophysiol* 68: 1384–1400, 1992.

METZNER W, KOCH C, WESSEL R, AND GABBIANI F. Feature extraction of burst-like spike patterns in multiple sensory maps. *J Neurosci* 15: 2283–2300, 1998.

MICKUS T, JUNG HY, AND SPRUSTON N. Properties of slow, cumulative sodium channel inactivation in rat hippocampal CA1 pyramidal neurons. *Biophys J* 76: 846–860, 1999.

MORENO H, KENTROS C, BUENO E, WEISER M, HERNANDEZ A, VEGA-SAENZ DE MIERA E, PONCE A, THORNHILL W, AND RUDY B. Thalamocortical projections have a K^+ channel that is phosphorylated and modulated by cAMP-dependent protein kinase. *J Neurosci* 15: 5486–5501, 1995.

NELSON ME. A mechanism for neuronal gain control by descending pathways. *Neural Comp* 6: 255–269, 1994.

NELSON ME, XU Z, AND PAYNE JR. Characterization and modeling of P-type electrosensory afferent responses to amplitude modulations in a wave-type electric fish. *J Comp Physiol [A]* 181: 532–544, 1997.

NOONAN LM, MORALES E, RASHID AJ, DUNN RJ, AND TURNER RW. Kv3.3 channels have multiple roles in regulating somatic and dendritic spike discharge (Abstract). *XXX Proc Soc Neurosci* 26: 1638, 2000.

Nuñez A, Amzica F, and Steriade M. Voltage-dependent fast (20–40 Hz) oscillations in long-axoned neocortical neurons. *Neuroscience* 51: 7–10, 1992.

Nuñez A, Amzica F, and Steriade M. Electrophysiology of cat association cortical cells in vivo: intrinsic properties and synaptic responses. *J Neurophysiol* 70: 418–430, 1993.

Pape HC. Queer current and pacemaker: the hyperpolarization-activated cation currents. *Annu Rev Physiol* 58: 329–348, 1996.

Paré D, Pape H, and Dong J. Bursting and oscillating neurons of the basolateral amygdaloid complex in vivo: electrophysiological properties and morphological features. *J Neurophysiol* 74: 1179–1191, 1995.

Paré D, Shink E, Gaudreau H, Destexhe A, and Lang EJ. Impact of spontaneous synaptic activity on the resting properties of cat neocortical neurons in vivo. *J Neurophysiol* 79: 1450–1460, 1998.

Parri HR and Crunelli V. Sodium current in rat and cat thalamocortical neurons: role of a non-inactivating component in tonic and burst firing. *J Neurosci* 18: 854–867, 1998.

Perney TM and Kaczmarek LK. Localization of a high threshold potassium channel in the rat cochlear nucleus. *J Comp Neurol* 386: 178–202, 1997.

Pinsky P and Rinzel J. Intrinsic and network rhythmogenesis in a reduced Traub model for CA3 neurons. *J Comput Neurosci* 1: 39–60, 1994.

Quadroni R and Knopfel T. Compartmental models of type A and type B guinea pig medial vestibular neurons. *J Neurophysiol* 72: 1911–1934, 1993.

Rapp M, Yarom Y, and Segev I. Modeling back propagating action potential in weakly excitable dendrites of neocortical pyramidal cells. *Proc Natl Acad Sci USA* 93: 11985–11990, 1996.

Rashid AJ, Morales E, Turner RW, and Dunn RJ. Dendritic Kv3 K$^+$ channels regulate burst threshold in a sensory neuron. *J Neurosci* 21: 125–135, 2001.

Ratnam R and Nelson ME. Nonrenewal statistics of electrosensory afferent spike trains: implications for the detection of weak sensory signals. *J Neurosci* 20: 6672–6683, 2000.

Rhodes P and Gray C. Simulations of intrinsically bursting neocortical pyramidal neurons. *Neural Comp* 6: 1086–1110, 1994.

Ribary U, Ioannides K, Singh K, Hasson R, Bolton J, Lado F, Mogilner A, and Llinás R. Magnetic field tomography of coherent thalamocortical 40-Hz oscillation in humans. *Proc Natl Acad Sci USA* 88: 11037–11041, 1991.

Rinzel J. A formal classification of bursting mechanisms in excitable systems. In: *Proc. Intl. Congress Mathematicians,* edited by Gleason AM. Providence, RI: Am. Math. Soc., 1987, p. 1578–1594.

Rudy B, Chow A, Lau D, Amarillo Y, Ozaita A, Saganich M, Moreno H, Nadal MS, Hernandez-Pineda R, Hernandez-Cruz A, Erisir A, Leonard C, and Vega-Saenz de Miera E. Contributions of Kv3 channels to neuronal excitability. *Ann NY Acad Sci* 868: 304–343, 1999.

Sanchez R, Surkis A, and Christopher L. Voltage-clamp analysis and computer simulation of a novel cesium-resistant A-current in guinea pig laterodorsal tegmental neurons. *J Neurophysiol* 79: 3111–3126, 1998.

Schwindt PC and Crill WE. Amplification of synaptic current by persistent sodium conductance in apical dendrite of neocortical neurons. *J Neurophysiol* 74: 2220–2224, 1995.

Schwindt PC, O'Brien J, and Crill WE. Quantitative analysis of firing properties of pyramidal neurons from layer 5 of rat sensorimotor cortex. *J Neurophysiol* 77: 2484–2498, 1997.

Sekirnjak C, Martone ME, Weiser M, Deerinck T, Bueno E, Rudy B, and Ellisman M. Subcellular localization of the K$^+$ channel subunit Kv3.1b in selected rat CNS neurons. *Brain Res* 766: 173–187, 1997.

Shao L-R, Halvorsrud R, Borg-Graham L, and Strom J. The role of BK-type Ca^{2+} dependent K$^+$ channels in spike broadening during repetitive firing in rat hippocampal pyramidal cells. *J Physiol (Lond)* 521: 135–146, 1999.

Shumway C. Multiple electrosensory maps in the medulla of weakly electric gymnotiform fish. I. Physiological differences. *J Neurosci* 9: 4388–4399, 1989.

Stafstrom C, Schwindt PC, Chub M, and Crill WE. Properties of persistent sodium conductance and calcium conductance of layer V neurons form cat sensorimotor cortex in vivo. *J Neurophysiol* 53: 153–170, 1985.

Stanford I, Traub R, and Jefferys J. Synaptic and intrinsic mechanism underlying spike doublets in oscillating subicular neurons. *J Neurophysiol* 80: 162–171, 1998.

Steriade M, Timofeev I, Dürmüller N, and Grenier F. Dynamic properties of corticothalamic neurons and local cortical interneurons generating fast rhythmic (30–40 Hz) spike bursts. *J Neurophysiol* 79: 483–490, 1998.

Stuart G and Häusser M. Initiation and spread of sodium action potentials in cerebellar Purkinje cells. *Neuron* 13: 703–712, 1994.

Stuart G and Sakmann B. Active propagation of somatic action potentials into neocortical pyramidal cell dendrites. *Nature* 367: 69–72, 1994.

Stuart G and Sakmann B. Amplification of EPSPs by axosomatic sodium channels in neocortical pyramidal neurons. *Neuron* 15: 1065–1076, 1995.

Stuart G, Schiller J, and Sakmann B. Action potential initiation and propagation in rat neocortical pyramidal neurons. *J Physiol (Lond)* 505: 617–632, 1997a.

Stuart G, Spruston N, Sakmann B, and Häusser M. Action potential initiation and backpropagation in neurons of the mammalian CNS. *Trends Neurosci* 20: 125–131, 1997b.

Traub R, Wong R, Miles R, and Michelson H. A model of a CA3 hippocampal neuron incorporating voltage-clamp data on intrinsic conductances. *J Neurophysiol* 66: 635–650, 1994.

Turner RW and Maler L. Oscillatory and burst discharge in the apteronotid electrosensory lateral line lobe. *J Exp Biol* 202: 1255–1265, 1999.

Turner RW, Maler L, Deerinck T, Levinson SR, and Ellisman M. TTX-sensitive dendritic sodium channels underlie oscillatory discharge in a vertebrate sensory neuron. *J Neurosci* 14: 6453–6471, 1994.

Turner RW, Meyers DER, Richardson TL, and Barker JL. The site for initiation of action potential discharge over the somato-dendritic axis of rat hippocampal CA1 pyramidal neurons. *J Neurosci* 11: 2270–2280, 1991.

Turner RW, Plant J, and Maler L. Oscillatory and burst discharge across electrosensory topographic maps. *J Neurophysiol* 76: 2364–2382, 1996.

Velasco I, Beck EJ, and Covarrubias M. Receptor-coupled regulation of K$^+$ channel N-type inactivation. *Neurobiology* 6: 23–32, 1998.

Wang L-Y, Gan L, Forsythe ID, and Kaczmarek LK. Contribution of the Kv3.1 potassium channel to high-frequency firing in mouse auditory neurones. *J Physiol (Lond)* 509: 183–194, 1998.

Wang X-J. Fast burst firing and short-term synaptic plasticity: a model of neocortical chattering neurons. *Neuroscience* 89: 347–362, 1999.

Wang X-J and Rinzel J. Oscillatory and bursting properties of neurons. In: *The Handbook of Brain Theory and Neural Networks,* edited by Arbib M. Cambridge, MA: MIT Press, 1996, p. 686–691.

Weiser M, de Miera V-S, Kentros C, Moreno H, Franzen L, Hillman D, and Baker H. Differential expression of Shaw-related K$^+$ channels in rat central nervous system. *J Neurosci* 14: 949–972, 1994.

Wessel R, Koch C, and Gabbiani F. Coding of time varying electric field amplitude modulations in a wave-type electric fish. *J Neurophysiol* 75: 2280–2293, 1996.

Williams S and Stuart G. Mechanisms and consequences of action potentials burst firing rat neocortical pyramidal neurons. *J Physiol (Lond)* 521: 467–482, 1999.

Williams SR and Stuart GJ. Action potential backpropagation and somato-dendritic distribution of ion channels in thalamocortical neurons. *J Neurosci* 20: 1307–1317, 2000.